

# Hydraulic control of mammalian embryo size and cell fate

Chii Jou Chan<sup>1\*</sup>, Maria Costanzo<sup>1</sup>, Teresa Ruiz-Herrero<sup>2</sup>, Gregor Mönke<sup>1</sup>, Ryan J. Petrie<sup>3</sup>, Martin Bergert<sup>1</sup>, Alba Diz-Muñoz<sup>1</sup>, L. Mahadevan<sup>2,4,5,6\*</sup> & Takashi Hiragi<sup>1,7\*</sup>

**Size control is fundamental in tissue development and homeostasis<sup>1,2</sup>. Although the role of cell proliferation in these processes has been widely studied, the mechanisms that control embryo size—and how these mechanisms affect cell fate—remain unknown. Here we use the mouse blastocyst as a model to unravel a key role of fluid-filled lumen in the control of embryo size and specification of cell fate. We find that there is a twofold increase in luminal pressure during blastocyst development, which translates into a concomitant increase in cell cortical tension and tissue stiffness of the trophoctoderm that lines the lumen. Increased cortical tension leads to vinculin mechanosensing and maturation of functional tight junctions, which establishes a positive feedback loop to accommodate lumen growth. When the cortical tension reaches a critical threshold, cell–cell adhesion cannot be sustained during mitotic entry, which leads to trophoctoderm rupture and blastocyst collapse. A simple theory of hydraulically gated oscillations recapitulates the observed dynamics of size oscillations, and predicts the scaling of embryo size with tissue volume. This theory further predicts that disrupted tight junctions or increased tissue stiffness lead to a smaller embryo size, which we verified by biophysical, embryological, pharmacological and genetic perturbations. Changes in luminal pressure and size can influence the cell division pattern of the trophoctoderm, and thereby affect cell allocation and fate. Our study reveals how luminal pressure and tissue mechanics control embryo size at the tissue scale, which is coupled to cell position and fate at the cellular scale.**

Luminal pressure is known to shape the early development of vasculature, the renal system and endocrine organs<sup>3,4</sup>, but our understanding of how luminal pressure affects tissue size—and how these are coordinated with cell fate—remains limited. In this study we sought to understand the interplay between lumen morphogenesis, embryo size and fate specification during blastocyst development in the mouse, which is conserved across mammalian species<sup>5</sup>. As the fluid-filled cavity forms and expands, the cells in the embryo segregate into the extra-embryonic trophoctoderm (which lines the cavity) and the inner cell mass (ICM) (Fig. 1a, Extended Data Fig. 1a); the trophoctoderm eventually gives rise to the placenta, and part of the ICM develops into the embryo proper<sup>6,7</sup>. Following this process dynamically, we observed that the blastocyst cavity shows an initial steady increase in volume, which is followed by a transition to an intermittent mode that is characterized by growth and sudden collapse; these events become more frequent towards the late blastocyst stage (embryonic day (E)4.5) (Fig. 1a, Supplementary Video 1), as has previously been reported<sup>8</sup>. Given that pre-implantation development occurs within a stiff glycoprotein coat (known as the zona pellucida), the size of the blastocyst may potentially be constrained by the zona pellucida. However, blastocysts without the zona pellucida, or those that form after embryo dissociation and re-aggregation (4× quarter (1/4) embryos), display cycles of expansion and collapse until they reach a size that is similar to that of blastocysts

with the zona pellucida (Fig. 1b, Extended Data Fig. 1b, Supplementary Video 2). Furthermore, the distributions of inter-collapse intervals for blastocysts with and without the zona pellucida are similar (Fig. 1c), which suggests that the zona pellucida does not influence the dynamics of blastocyst collapse and the final size of the blastocyst, and argues for an autonomous mechanism for the control of blastocyst size.

Given that the blastocyst is a fluid-filled tissue shell, we hypothesized that the luminal pressure and tissue stress of trophoctoderm may regulate blastocyst size. Using a micropressure probe<sup>9</sup>, we directly measured the hydrostatic pressure in a developing mouse embryo (Extended Data Fig. 2). Mid-stage blastocysts (E4.0) have a luminal pressure of approximately 650 Pa, which increases to about 1,500 Pa by the mature blastocyst stage (E4.5) (Fig. 1d), consistent with a recent report<sup>10</sup>. By contrast, blastocysts without the zona pellucida show a lower pressure (Fig. 1d, red), which indicates that there is an additional build-up of pressure due to the constricting nature of the zona pellucida. When we bisected the embryos at 4-cell stage, the resulting E4.5 halved (1/2) blastocysts were found to display a lower pressure than whole (1×) blastocysts (Fig. 1d, blue). Using micropipette aspiration<sup>11</sup>, we measured a progressive increase in the cortical tension of trophoctoderm cells for blastocysts of a range of sizes (1/4, 1/2, 3/4 and 1×) during development (Fig. 1e). Notably, although trophoctoderm cells in the reduced blastocysts exhibit higher cortical tension than those in the whole embryos at E3.5, by E4.5 (when they reach their steady-state size) the cortical tension in these cells converges to a value similar to that of cells from the whole embryos (about 1,100 pN μm<sup>-1</sup>). This suggests that hydraulically generated tissue yield stress may set a threshold size for the mature blastocysts.

We next quantified changes in trophoctoderm cell shape during blastocyst development. We found that the cortical tension of trophoctoderm cells scales well with cell deformation across all stages and sizes (Fig. 1f, Extended Data Fig. 1c), which suggests that the trophoctoderm cells behave as linearly elastic materials. The correlation between cortical tension and changes in cell shape suggests that luminal expansion affects trophoctoderm-cell mechanics globally via cell stretching, in a cell-non-autonomous manner. To confirm this causality, we first perturbed cavity expansion by pharmacologically blocking fluid influx or inducing fluid leakage. Impaired function of Na<sup>+</sup>/K<sup>+</sup> ATPase pumps by ouabain<sup>12</sup> or of tight-junction protein claudins by *Clostridium perfringens* enterotoxin (CPE)<sup>13</sup> led to reduced cavity size (Extended Data Fig. 7e) and reduced cortical tension of trophoctoderm cells (Fig. 2a). Physical manipulation of cavity size by mechanical inflation (or deflation) also led to a transient increase (or decrease) in the cortical tension of trophoctoderm cells (Fig. 2b). These data indicate that cavity expansion drives changes in tissue and cell geometry, which in turn increases the cortical tension of trophoctoderm cells.

On the molecular level, we observed extensive cytoskeletal remodelling at trophoctoderm cell–cell junctions after lumen expansion (Fig. 2c). Occludin, a transmembrane tight-junction protein, shows

<sup>1</sup>European Molecular Biology Laboratory, Heidelberg, Germany. <sup>2</sup>Paulson School of Engineering and Applied Sciences, Harvard University, Cambridge, MA, USA. <sup>3</sup>Department of Biology, Drexel University, Philadelphia, PA, USA. <sup>4</sup>Department of Physics, Harvard University, Cambridge, MA, USA. <sup>5</sup>Department of Organismic and Evolutionary Biology, Harvard University, Cambridge, MA, USA. <sup>6</sup>Kavli Institute for Bionano Science and Technology, Harvard University, Cambridge, MA, USA. <sup>7</sup>Institute for the Advanced Study of Human Biology (WPI-ASHBi), Kyoto University, Kyoto, Japan. \*e-mail: cchan@embl.de; lmahadev@g.harvard.edu; hiragi@embl.de

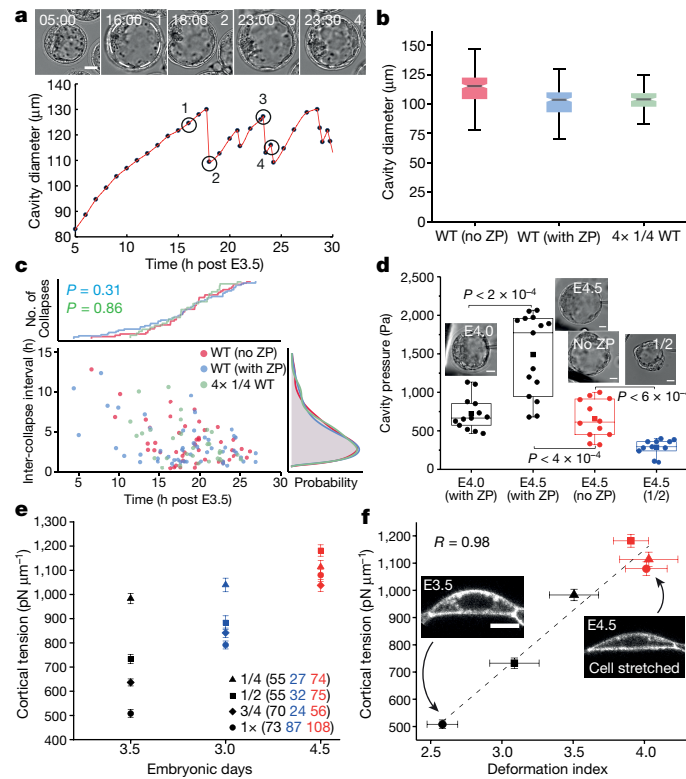


**Fig. 1 | Blastocyst development is driven by increased luminal pressure and cortical tension of trophectoderm.** **a**, Top, images of a blastocyst with intact zona pellucida undergoing blastocyst expansion (representative data from four independent experiments). Dotted circle denotes cavity. Time is shown as h:min after E3.5. Bottom, corresponding plot of cavity diameter with time. E3.5, 84 h after injection with human chorionic gonadotropin. **b**, Cavity diameter at the plateau stage for wild-type (WT) blastocysts with ( $n = 13$  embryos) and without ( $n = 14$  embryos) zona pellucida (ZP), and for aggregated embryos ( $n = 13$  embryos). **c**, Inter-collapse interval as a function of time for embryos in **b**. Kolmogorov–Smirnov test (two-tailed).  $P = 0.31$  for wild-type (with zona pellucida) embryos;  $P = 0.86$  for  $4 \times$  quarter ( $1/4$ ) embryos compared to wild-type (without zona pellucida) embryos.

a change in localization from the cytoplasm to the tight junctions, and di-phosphorylated myosin regulatory light chains (ppMRLC) show a shift from punctate to continuous localization at the same site (Extended Data Fig. 3a). Vinculin, a known tension sensor *in vitro*<sup>14</sup>, also shows strong enrichment at the tight junctions after blastocyst maturation. Notably, mechanical deflation and ouabain treatment lead to the disassembly of vinculin from tight junctions (Fig. 2d), which suggests that vinculin may be mechanosensitive to luminal expansion (Extended Data Fig. 3e–h). Specific localization of ppMRLC, MYH9 and vinculin at tight junctions (Extended Data Fig. 3a–d) further suggests that tight junctions are probably the stress-bearing sites during blastocyst expansion—unlike other epithelia in culture or tissues, in which vinculin and active myosin are localized at adherens junctions<sup>15,16</sup>. Importantly, reduced cortical tension leads to disrupted tight-junction seals (Fig. 2e, f), which suggests that a positive feedback loop that links cortical tension and tight-junction maturation may function to allow the blastocyst to accommodate pressure growth during development.

The presence of a cortical tension threshold at which the mature blastocysts exhibit intermittent collapse implies a critical failure stress in the trophectoderm. We observed that blastocyst collapse is often preceded by mitosis of mural trophectoderm cells (Fig. 3a, Extended Data Fig. 4a), which suggests that collapses may be triggered by junctional loss through cell rounding. Indeed, embryos arrested at the S-phase entry by aphidicolin showed no collapse compared to controls (Fig. 3b, top, Extended Data Fig. 4b, c, Supplementary Videos 3, 4) but started to exhibit collapse upon washout (Supplementary

**d**, Cavity pressure of whole blastocysts at various stages with and without zona pellucida, and for half ( $1/2$ ) blastocysts at E4.5. Scale bars,  $20 \mu\text{m}$ . Mann–Whitney  $U$  test. **e**, Cortical tension of trophectoderm in blastocysts of various sizes, measured during early (black), middle (blue) and late blastocyst stage (red). Numbers in parentheses indicate the number of cells. **f**, Cortical tension as a function of deformation index (basal area of trophectoderm cell divided by cell volume<sup>2/3</sup>). Colours and symbols correspond to those in **e**.  $n$  (for E3.5) = 36, 45 and 46 embryos for  $1/4$ ,  $1/2$  and whole ( $1 \times$ ) embryos, respectively;  $n$  (for E4.5) = 53, 58 and 49 embryos for  $1/4$ ,  $1/2$  and  $1 \times$  embryos, respectively.  $R$ , Pearson test. Mean  $\pm$  s.e.m. (**e**, **f**). Scale bar,  $20 \mu\text{m}$ . Box plots in **b**, **d** show median, 25th and 75th percentiles, and whiskers extending to maximum and minimum data points.

Video 5). By contrast, embryos treated with nocodazole and arrested at the M-phase showed constant fluid leakage and did not expand (Fig. 3b, bottom, Extended Data Fig. 4d, Supplementary Video 6), which could be rescued by washout (Extended Data Fig. 4e). Notably, we rarely find collapse events in the early and mid-blastocyst stage (Fig. 1a, c) despite extensive cell divisions, which suggests that a high cortical tension may be required to ‘prime’ junctional rupture upon mitosis. Consistent with this, we measured a higher cortical tension (Extended Data Fig. 4f) in the mitotic cells of late blastocysts compared to that in the early blastocysts. Furthermore, abolishment of actomyosin contractility using myosin inhibitor blebbistatin (Bb(-)), or enhancement of it via treatment with calyculin A led to suppression or promotion of blastocyst collapse, respectively (Fig. 3c–e, Supplementary Videos 7, 8). Finally, reduced blastocysts—which exhibit higher cortical tension at the early blastocyst stage (Fig. 1e, Supplementary Video 9)—displayed earlier and more-frequent collapses compared to the whole blastocysts (Fig. 3f, Extended Data Fig. 5a). These results show that high cortical tension coupled with mitotic cell rounding leads to blastocyst collapse.

Together, our findings suggest that blastocyst size is governed by feedback mechanisms that operate across multiple scales (Fig. 4a). These findings are consistent with a recently proposed theory<sup>17</sup> for control of cyst size on the basis of hydraulically gated oscillations. Here we model the blastocyst as a spherical shell that is subjected to an osmotic imbalance that creates an inward flux of solvent. The balance between osmotic and hydrostatic pressure determines the frequency of size oscillations and the average size as a function of

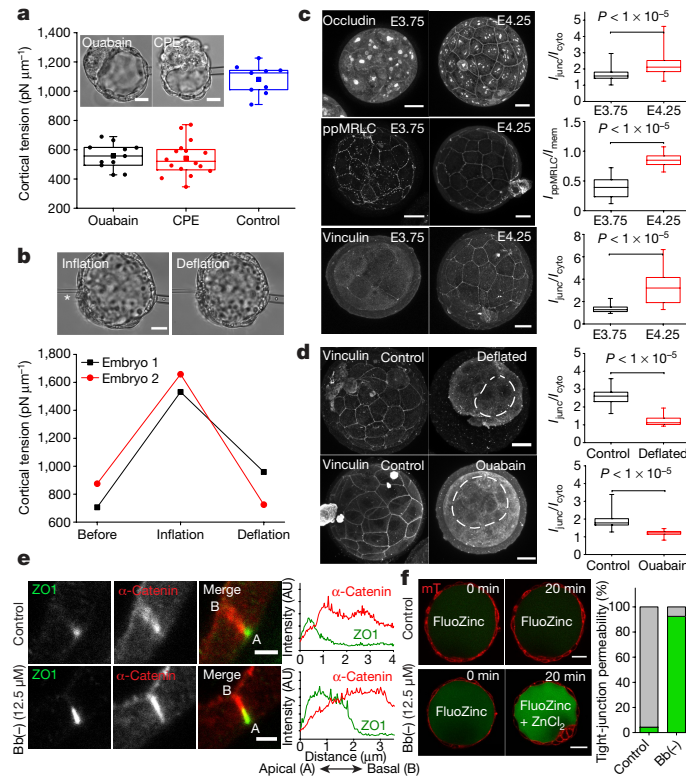


**Fig. 2 | Luminal expansion promotes junctional maturation.** **a**, Cortical tension of trophoblast cells in ouabain-treated ( $n = 14$  cells from 5 embryos) and CPE-treated ( $n = 16$  cells from 7 embryos) embryos, compared to controls ( $n = 9$  cells from 4 embryos). Scale bars, 20  $\mu\text{m}$ . **b**, Cortical tension of trophoblast cells from two blastocysts following mechanical inflation and deflation of cavity at short timescales (~30 s). Asterisk marks the injection needle. Scale bar, 20  $\mu\text{m}$ . **c**, Immunostaining of occludin, ppMRLC and vinculin at early (E3.75) and late (E4.25) blastocyst stages. Corresponding box plots are shown on the right (occludin,  $n = 114$  cells from 18 embryos; ppMRLC,  $n = 67$  cells from 52 embryos; vinculin,  $n = 53$  cells from 23 embryos).  $I_{\text{junc}}$ ,  $I_{\text{cyto}}$ ,  $I_{\text{ppMRLC}}$  and  $I_{\text{mem}}$  are the integrated densities of the junction, cytoplasm, ppMRLC and membrane markers, respectively. **d**, Immunostaining of vinculin in mechanically deflated and ouabain-treated embryos at E4.25 (dotted lines

tissue elastic modulus, rupture stress, tissue permeability and osmotic pressure (Supplementary Notes). A key prediction of the theory is that the ultimate size of blastocyst ( $R_{\text{max}}$ ) scales with the initial size of the blastocyst ( $R_0$ ); that is,  $R_{\text{max}} \sim (1 + (\sigma_c - \sigma_0)/E) \times R_0$ , in which  $\sigma_c$  is the trophoblast rupture stress,  $\sigma_0$  is the stress before cavitation and  $E$  is the elastic modulus of trophoblast. Using blastocysts of different sizes, we confirmed this linear scaling relationship experimentally (Fig. 4b). Furthermore, using the measured values of luminal pressure ( $P \sim 650$  Pa), cavity radius ( $R \sim 60$   $\mu\text{m}$ ) and shell thickness ( $h \sim 3$   $\mu\text{m}$ ) at E4.5, we obtain a lower bound for the rupture stress, given by  $\sigma_c = PR/2h$ . From the slope, we then estimate  $E$  to be about 7 kPa at E4.5, which is close to the apparent trophoblast stiffness of mature blastocysts measured by atomic force microscopy (Fig. 4c, Extended Data Fig. 6) and comparable to that of cell monolayers or cysts<sup>18,19</sup>. Notably, we found that the trophoblast stiffens during blastocyst development (Fig. 4c), possibly owing to junctional maturation from myosin enrichment (Fig. 2c); this has also been observed in cell culture and *Drosophila* wing disc<sup>20,21</sup>. Incorporating this finding by generalizing our model<sup>17</sup> to account for an elasto-plastic constitutive law (Supplementary Notes), we predict that leaky cell junctions lead to a delay and less-frequent collapses, whereas increased cortical tension (hence increased  $E$ ) leads to earlier onset of, and more-frequent, collapses (Fig. 4d, e). This simple theoretical framework qualitatively captured the dynamics of blastocyst size oscillation in these two conditions (Fig. 3c–e), independently of the molecular details.

denote cavities). Corresponding box plots are shown on the right (deflated,  $n = 43$  cells from 20 embryos; ouabain,  $n = 87$  cells from 33 embryos). Scale bars, 20  $\mu\text{m}$ . Mann–Whitney  $U$  test. **e**, Immunostaining of ZO1 and  $\alpha$ -catenin in control blastocysts versus blastocysts treated with Bb(-) (at E4.25). Line scans are shown on the right. AU, arbitrary units. Scale bars, 20  $\mu\text{m}$ . **f**, Tight-junction permeability assay assesses tight-junction sealing (see Methods). Left, blastocysts treated with Bb(-) (bottom) showed enhanced signals in the cavity, owing to impaired tight-junction sealing and  $\text{ZnCl}_2$  penetration. Right, percentage of blastocysts showing increased permeability (green) in embryos treated with Bb(-) ( $n = 28$  embryos) compared to control embryos ( $n = 23$  embryos). Scale bars, 30  $\mu\text{m}$ . In **b** and **e**, representative examples of four independent experiments are shown. All box plots show median, 25th and 75th percentiles, and whiskers extending to maximum and minimum data points.

Leaky cell junctions also led to reduced expansion rate and blastocyst size, as shown by pharmacological inhibition of actomyosin contractility (Extended Data Fig. 7a, b, g, h) and by heterozygous (*Myh9*<sup>+/-</sup>) embryos derived from maternal homozygous ( $m^{-/-}$ ) or maternal heterozygous ( $m^{+/-}$ ) mice ( $m^{-/-}$  *Myh9*<sup>+/-</sup> and  $m^{+/-}$  *Myh9*<sup>+/-</sup> hereafter) that have reduced cortical tension<sup>22</sup> (Extended Data Figs. 7a, b, 8a–c, Supplementary Video 10). Importantly, reduced expansion in these perturbed embryos is not due to reduced cell proliferation (Extended Data Fig. 7c, f, i, 8d), which can influence the expansion rate (Extended Data Fig. 5b–d). The theory further predicts that softening (or stiffening) the trophoblast shell leads to an increase (or decrease) in the expansion rate and size. Consistent with this prediction, we found that treatment with ECCD1—an E-cadherin-blocking antibody that weakens cell–cell adhesion and tissue stiffness<sup>20,23</sup>—led to increased cavity growth (Extended Data Figs. 7d–f, 9d, e). By contrast, treatment with lysophosphatidic acid<sup>24</sup> and calyculin A, both of which activate cortical contractility, led to a reduced expansion rate and size (Extended Data Fig. 9a–c, Supplementary Video 11), possibly through tissue stiffening.

Changes in blastocyst size with unchanged cell numbers necessarily affect tissue architecture. Indeed, we found that in embryos with smaller cavities (Bb(-),  $m^{-/-}$  *Myh9*<sup>+/-</sup>,  $m^{+/-}$  *Myh9*<sup>+/-</sup>, CPE, ouabain and hypertonic), more cells were allocated to the inner layer of the blastocyst, which resulted in a higher ratio of ICM to trophoblast cells, whereas embryos with larger cavities (ECCD1) exhibited

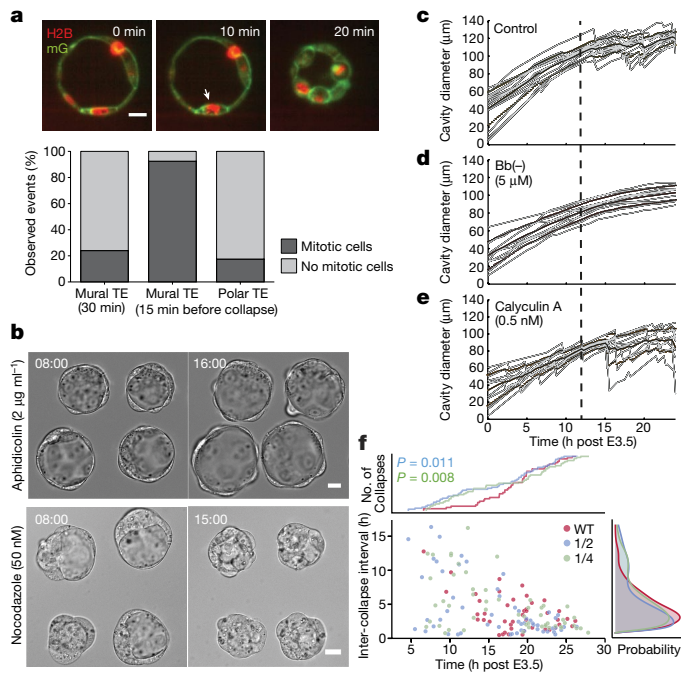


**Fig. 3 | Stretch-induced cortical stiffening and mitosis collectively lead to blastocyst collapse.** **a**, Blastocyst collapse is triggered by mitosis of mural trophoctoderm (TE) cells. Top, representative image of an H2B–mCherry–mG mouse embryo showing mitotic cell rounding (white arrow) before blastocyst collapse. Bottom, quantification of events in which mitotic or no mitotic cells are observed before blastocyst collapse. Scale bar, 20  $\mu\text{m}$ . **b**, Top, images of aphidicolin-treated 1/2 blastocysts, which expanded without collapse even 16 h after E3.5. Bottom, images of nocodazole-treated 1/2 blastocysts, which showed constant leakage and failed expansion. Scale bars, 20  $\mu\text{m}$ . Images show representative examples of four independent experiments. **c–e**, Cavity diameter as a function of time for embryos treated with Bb(–) ( $n = 10$  embryos) (**d**) and calyculin A ( $n = 11$  embryos) (**e**) compared to controls ( $n = 13$  embryos) (**c**). Solid black lines denote mean diameter with  $\pm$  s.d. denoted by dotted lines. Grey lines represent the evolution of cavity size for individual embryos. Bold dashed line indicates 12 h after E3.5. **f**, Inter-collapse interval as a function of time for embryos of various sizes. Kolmogorov–Smirnov test (two-tailed).  $P = 0.011$  for 1/2 embryos;  $P = 0.008$  for 1/4 embryos, compared to 1 $\times$  embryos.  $n = 14, 21, 16$  embryos for 1 $\times$ , 1/2 and 1/4 embryos, respectively.

a decreased ratio of ICM to trophoctoderm cells (Fig. 5a, b, Extended Data Fig. 8e). Although reduced contractility may affect cell sorting<sup>22</sup>, changes to cavity size owing to reduced fluid influx (CPE, ouabain and hypertonic conditions) or trophoctoderm stiffness (ECCD1 treatment) can independently alter lineage composition. Of note, embryos with a reduced cavity size occasionally did not spatially segregate into the inner and outer cells, as shown by CDX2-positive cells in the ICM (Fig. 5a, Extended Data Fig. 8f). This raises the possibility that reduced lumen expansion may facilitate outer cell internalization. Indeed, using a DiI dye assay to track outer cells during blastocyst development (Extended Data Fig. 10a), we found more DiI-positive cells in the ICM of hypertonic-treated embryos (at E4.5) compared to control (Fig. 5c, Extended Data Fig. 10b). Furthermore, in the case of hypertonic treatments, we observed more events in which an outer cell underwent asymmetric division to generate one trophoctoderm-forming and one ICM-forming cell (Fig. 5d, Supplementary Videos 12, 13). The ICM-forming cells eventually downregulate their CDX2 expression, whereas cells that remain outside the ICM maintain or upregulate their CDX2 expression (Fig. 5d, Extended Data Fig. 10c). Downregulation of CDX2 is possibly due to a lack of contact-free surface and apical domain acquisition, which leads to differential Yap signalling and cell-fate specification<sup>25,26</sup>. Overall, our results provide strong evidence that luminal pressure and cavity size can influence trophoctoderm cell shape and division pattern—possibly through

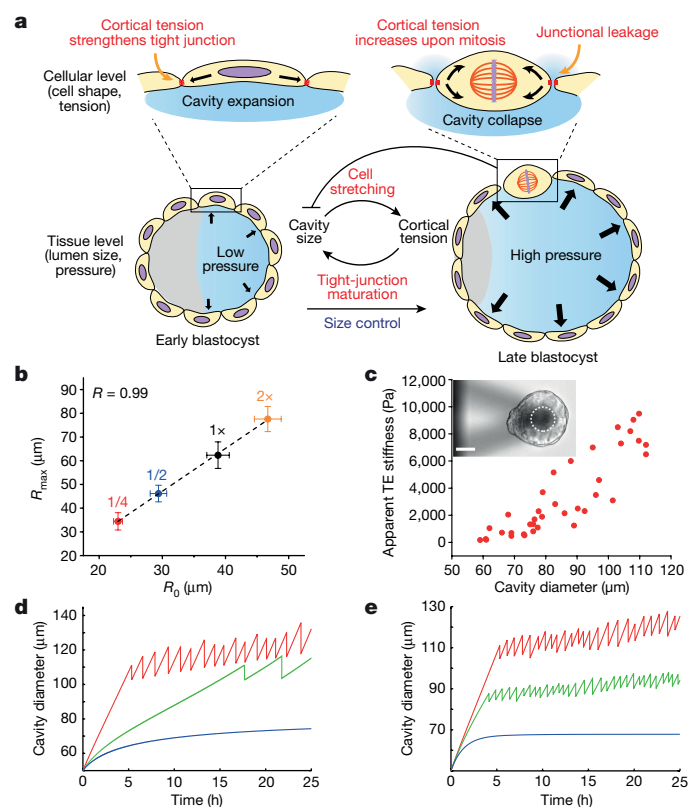


**Fig. 4 | Physical model predicts the change in blastocyst size and oscillation dynamics with perturbed cortical tension.** **a**, Schematic representing how multi-scale feedback mechanisms between luminal pressure and tissue mechanics control the size of blastocysts. Luminal pressure stretches cells and generates mechanical stress at the tissue scale, which reinforces junctional maturation through mechanosensing at the cellular scale. As tissue stress reaches a critical threshold, cell–cell adhesion cannot be sustained during mitosis, which triggers junctional rupture and the collapse of the blastocyst cavity. Tight junctions then re-seal and the blastocyst expands again, and the whole process repeats itself to generate size oscillations. **b**, Steady-state blastocyst radius as a function of the initial embryo radius.  $n = 16, 16, 22$  and 7 embryos for 1/4, 1/2, 1 $\times$  and double (2 $\times$ ) embryos, respectively.  $R$ , Pearson test. Mean  $\pm$  s.d. **c**, Apparent trophoctoderm stiffness (Young’s modulus) as a function of cavity radius, measured by atomic force microscopy.  $n = 37$  embryos (of various stages) pooled from four independent experiments. Inset, bright-field image of a blastocyst under indentation. Dotted circle indicates bead (50- $\mu\text{m}$  diameter) glued to the cantilever. Scale bar, 40  $\mu\text{m}$ . **d**, Theoretical model predicts a delay or abolishment of steady-state oscillations in response to leakage.  $J_{\text{leak}} = 0 \mu\text{m h}^{-1}$  (red),  $5.5 \mu\text{m h}^{-1}$  (green) and  $7.5 \mu\text{m h}^{-1}$  (blue). **e**, Theoretical model predicts an earlier onset of, and more frequent, collapses in response to increased cortical tension and tissue stiffness.  $E = 5 \text{ kPa} + 2.5\sigma$  and  $E_p = 50 \text{ kPa}$  (red),  $E = 10 \text{ kPa} + 3\sigma$  and  $E_p = 64 \text{ kPa}$  (green) and  $E = 20 \text{ kPa} + 5\sigma$  and  $E_p = 84 \text{ kPa}$  (blue).

mechanical means<sup>27</sup>—and thereby affect fate specification (Extended Data Fig. 10d).

Our study has identified luminal pressure as a long-range mechanical signal that coordinates cellular response and tissue self-organization across multiple scales. Our work further substantiates the notion that tissue-scale forces can have a critical role in shaping form (lumen size) and function (junctional maturation and cell fate) during embryogenesis<sup>28,29</sup>. Given the widespread presence of fluid-filled lumina in epithelial tissue morphogenesis (such as in the lung and kidney), it would seem natural to explore hydraulically mediated control of tissue size and cell fate in such systems.

### Online content

Any methods, additional references, Nature Research reporting summaries, source data, extended data, supplementary information, acknowledgements, peer review information; details of author contributions and competing interests; and statements of data and code availability are available at <https://doi.org/10.1038/s41586-019-1309-x>.

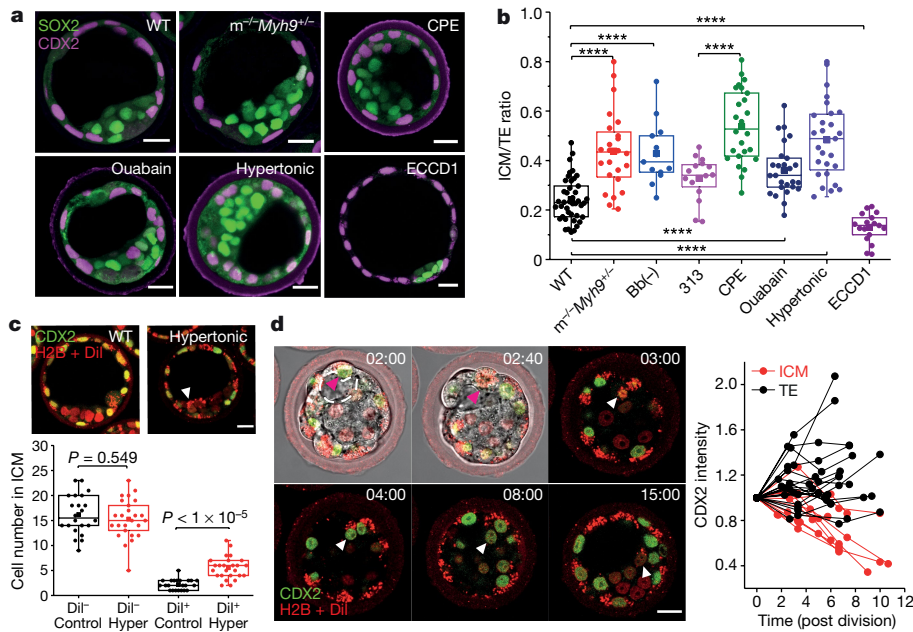


**Fig. 5 | Luminal pressure couples cell positioning and fate specification.**

**a**, Immunostaining of late blastocyst stage (E4.25) wild-type,  $m^{-/-} Myh9^{+/-}$ , and CPE-, ouabain-, hypertonic- and ECCD1-treated embryos, showing trophoctoderm (CDX2, magenta) and epiblast (SOX2, green) fate. Scale bars, 20  $\mu\text{m}$ . **b**, The ICM-to-trophectoderm cell ratio for E4.25 wild-type ( $n = 37$  embryos),  $m^{-/-} Myh9^{+/-}$  ( $n = 24$  embryos), Bb(-)-treated ( $n = 13$  embryos), CPE-treated ( $n = 26$  embryos), CPE313-treated (control;  $n = 16$  embryos), ouabain-treated ( $n = 26$  embryos), hypertonic-treated ( $n = 28$  embryos), and ECCD1-treated embryos ( $n = 17$  embryos). Mann-Whitney  $U$  test. \*\*\*\* $P < 1 \times 10^{-5}$ . **c**, Top, images of CDX2-GFP (green) and H2B-mCherry (red)-expressing control and hypertonic-treated (hyper) embryos at E4.5. White arrowhead indicates DiI-positive cells in the ICM. Scale bar, 20  $\mu\text{m}$ . Bottom, box plot of numbers of DiI-positive and DiI-negative cells within the ICM of

control embryos (black,  $n = 22$  embryos) and hypertonic-treated embryos (red,  $n = 25$  embryos) at E4.5. Mann-Whitney  $U$  test. **d**, Left, time-lapse images of a hypertonic-treated, DiI-labelled CDX2-GFP  $\times$  H2B-mCherry-expressing embryo undergoing blastocyst expansion (dotted line marks cavity). Asymmetric division of outer cells (magenta arrowhead) generates one trophoctoderm-forming and one ICM-forming cell (white arrowhead). Time is shown as h:min after E3.5. Scale bar, 20  $\mu\text{m}$ . Right, dynamics of normalized CDX2 expression in hypertonic-treated embryos for cells that remained outside the ICM (black,  $n = 20$  cells), and cells that internalized into the ICM after asymmetric division (red,  $n = 11$  cells). Data pooled from ten embryos over three independent experiments. In **a**, **c**, representative examples of three or more independent experiments are shown. Box plots show median, 25th and 75th percentiles, and whiskers extending to maximum and minimum data points.

Received: 20 August 2018; Accepted: 21 May 2019;  
Published online 12 June 2019.

- Conlon, I. & Raff, M. Size control in animal development. *Cell* **96**, 235–244 (1999).
- Day, S. J. & Lawrence, P. A. Measuring dimensions: the regulation of size and shape. *Development* **127**, 2977–2987 (2000).
- Navis, A. & Bagnat, M. Developing pressures: fluid forces driving morphogenesis. *Curr. Opin. Genet. Dev.* **32**, 24–30 (2015).
- Navis, A. & Nelson, C. M. Pulling together: tissue-generated forces that drive lumen morphogenesis. *Semin. Cell Dev. Biol.* **55**, 139–147 (2016).
- Rossant, J. & Tam, P. P. L. New insights into early human development: lessons for stem cell derivation and differentiation. *Cell Stem Cell* **20**, 18–28 (2017).
- Rossant, J. & Tam, P. P. L. Blastocyst lineage formation, early embryonic asymmetries and axis patterning in the mouse. *Development* **136**, 701–713 (2009).
- Wennekamp, S., Mesecke, S., Nédélec, F. & Hiiragi, T. A self-organization framework for symmetry breaking in the mammalian embryo. *Nat. Rev. Mol. Cell Biol.* **14**, 452–459 (2013).
- Niimura, S. Time-lapse videomicrographic analyses of contractions in mouse blastocysts. *J. Reprod. Dev.* **49**, 413–423 (2003).
- Petrie, R. J., Koo, H. & Yamada, K. M. Generation of compartmentalized pressure by a nuclear piston governs cell motility in a 3D matrix. *Science* **345**, 1062–1065 (2014).
- Leonavicius, K. et al. Mechanics of mouse blastocyst hatching revealed by a hydrogel-based microdeformation assay. *Proc. Natl Acad. Sci. USA* **115**, 10375–10380 (2018).
- Maitre, J. L., Niwayama, R., Turlier, H., Nédélec, F. & Hiiragi, T. Pulsatile cell-autonomous contractility drives compaction in the mouse embryo. *Nat. Cell Biol.* **17**, 849–855 (2015).
- Violette, M. I., Madan, P. & Watson, A. J.  $\text{Na}^+/\text{K}^+$ -ATPase regulates tight junction formation and function during mouse preimplantation development. *Dev. Biol.* **289**, 406–419 (2006).
- Moriwaki, K., Tsukita, S. & Furuse, M. Tight junctions containing claudin 4 and 6 are essential for blastocyst formation in preimplantation mouse embryos. *Dev. Biol.* **312**, 509–522 (2007).
- Grashoff, C. et al. Measuring mechanical tension across vinculin reveals regulation of focal adhesion dynamics. *Nature* **466**, 263–266 (2010).

- Yonemura, S., Wada, Y., Watanabe, T., Nagafuchi, A. & Shibata, M.  $\alpha$ -Catenin as a tension transducer that induces adherens junction development. *Nat. Cell Biol.* **12**, 533–542 (2010).
- Hara, Y., Shagirov, M. & Toyama, Y. Cell boundary elongation by non-autonomous contractility in cell oscillation. *Curr. Biol.* **26**, 2388–2396 (2016).
- Ruiz-Herrero, T., Alessandri, K., Gurchenkov, B. V., Nassoy, P. & Mahadevan, L. Organ size control via hydraulically gated oscillations. *Development* **144**, 4422–4427 (2017).
- Harris, A. R. et al. Characterizing the mechanics of cultured cell monolayers. *Proc. Natl Acad. Sci. USA* **109**, 16449–16454 (2012).
- Shen, Y. et al. Mechanical characterization of microengineered epithelial cysts by using atomic force microscopy. *Biophys. J.* **112**, 398–409 (2017).
- Harris, A. R., Daeden, A. & Charras, G. T. Formation of adherens junctions leads to the emergence of a tissue-level tension in epithelial monolayers. *J. Cell Sci.* **127**, 2507–2517 (2014).
- Duda, M. et al. Polarization of myosin II refines tissue material properties to buffer mechanical stress. *Dev. Cell* **48**, 245–260.e7 (2019).
- Maitre, J. L. et al. Asymmetric division of contractile domains couples cell positioning and fate specification. *Nature* **536**, 344–348 (2016).
- Shirayoshi, Y., Okada, T. S. & Takeichi, M. The calcium-dependent cell-cell adhesion system regulates inner cell mass formation and cell surface polarization in early mouse development. *Cell* **35**, 631–638 (1983).
- Ruprecht, V. et al. Cortical contractility triggers a stochastic switch to fast amoeboid cell motility. *Cell* **160**, 673–685 (2015).
- Nishioka, N. et al. The Hippo signaling pathway components Lats and Yap pattern Tead4 activity to distinguish mouse trophectoderm from inner cell mass. *Dev. Cell* **16**, 398–410 (2009).
- Korotkevich, E. et al. The apical domain is required and sufficient for the first lineage segregation in the mouse embryo. *Dev. Cell* **40**, 235–247.e7 (2017).
- Xiong, F. et al. Interplay of cell shape and division orientation promotes robust morphogenesis of developing epithelia. *Cell* **159**, 415–427 (2014).
- Gilmour, D., Rembold, M. & Leptin, M. From morphogen to morphogenesis and back. *Nature* **541**, 311–320 (2017).
- Chan, C. J., Heisenberg, C. P. & Hiiragi, T. Coordination of morphogenesis and cell-fate specification in development. *Curr. Biol.* **27**, R1024–R1035 (2017).

**Publisher's note:** Springer Nature remains neutral with regard to jurisdictional claims in published maps and institutional affiliations.

© The Author(s), under exclusive licence to Springer Nature Limited 2019

## METHODS

**Embryo work. Recovery and culture.** Animal work was performed in the animal facility at the European Molecular Biology Laboratory, with permission from the institutional veterinarian overseeing the operation (ARC number TH11 00 11). The animal facilities are operated according to international animal welfare rules (Federation for Laboratory Animal Science Associations guidelines and recommendations). (C57BL/6x3H) F1 and CDX2-GFP×H2B-mCherry mice were used. Mice were used from eight-weeks of age onwards.

Embryos were recovered from superovulated female mice mated with male mice. Superovulation was induced by intraperitoneal injection of 5 international units (IU) of pregnant mare's serum gonadotropin (Intervet Intergonan), followed by intraperitoneal injection of 5 IU human chorionic gonadotropin (Intervet Ovogest 1500) 44–48 h later. Embryos were recovered at both the 2-cell stage (E1.5) and at the 8-cell stage (E2.5), by flushing oviducts from plugged females with 37°C KSOMaa with HEPES (Zenith Biotech, ZEHP-050, 50 ml) using a custom-made syringe (Acufirm, 1400 LL 23). Embryos were handled using an aspirator tube (Sigma, A5177-5EA) equipped with glass pipettes pulled from glass micropipettes (Blaubrand intraMark). For *in vitro* culture, embryos were transferred to 10- $\mu$ l droplets of KSOM (Millipore, MR-121-D) in a tissue-culture dish (Falcon, 353001) covered with mineral oil (Sigma, M8410 or Acros Organics), and cultured in an incubator with a humidified atmosphere supplemented with 5% CO<sub>2</sub> at 37°C.

Embryos were dissected out of zona pellucidae at the 4-cell stage using a holding pipette and a glass needle<sup>30</sup>, or dissolved using pronase (0.5% protease (Sigma, P-8811) in KSOMaa with HEPES and 0.5% PVP-40). Embryos with the zona pellucida removed were cultured in Petri dishes (Falcon, 351008). For pressure measurement and micropipette aspiration, embryos with the zona pellucida removed were transferred to KSOMaa with HEPES covered with oil, in 50-mm glass-bottomed dishes (MatTek, P50G-1.5-14.F). For time-lapse imaging, embryos were transferred to KSOMaa with HEPES in 0.16–0.19-mm glass-bottomed dishes (MatTek, P35G-1.5-10-C).

**Reduced and double embryos.** Embryos at the 4-cell stage with the zona pellucida removed were washed in Ca<sup>2+</sup>-free KSOM and aspirated multiple times through a narrow glass pipette (with a radius comparable to that of the whole embryo). Dissociated blastomeres (1/4 embryos) were then washed multiple times in KSOM before being transferred to KSOM for culture. 1/2 embryos were made by placing two blastomeres in micro-indented wells filled with KSOM. Double embryos were made by placing two 4-cell-stage embryos in the micro-wells.

**Mouse lines and genotyping.** Embryos derived from mating between C57BL/6×C3H F1 hybrid strain were used for wild-type embryos. mTmG mice (Gt(ROSA)26Sortm4(ACTB-tdTomato,-EGFP)Luo)<sup>31</sup> or mG mice (after Cre-mediated excision of mT) were used to visualize plasma membranes, and H2B-GFP or H2B-mCherry mice<sup>32</sup> were used to visualize nuclei. Genes were deleted maternally using *Zp3-cre* (Tg(Zp3-cre)93Kw) mice<sup>33</sup>, to generate m<sup>-/-</sup> *Myh9*<sup>+/-</sup> embryos, B6C3F1 males were crossed with *Myh9*<sup>fl/fl</sup>/*Zp3-cre*<sup>+/-</sup> females<sup>22</sup>. To generate m<sup>+/-</sup> *Myh9*<sup>+/-</sup> embryos, B6C3F1 males were crossed with *Myh9*<sup>+/-</sup> females. To discriminate between wild-type and mutant embryos in the same littermate, embryos at the E4.25-blastocyst stage were genotyped following immunofluorescence staining and imaging. For genotyping of blastocysts, fixed or live blastocysts were lysed, followed by PCR with the following primers: *Myh9*EKFw3 (5'-TTGAGCCCTTCTTGACCTA-3'), *Myh9*EKRv3 (5'-GCCACATCTCAGCCTAGGAT-3'), *Myh9*EKDe11 (5'-CGGGAAGGAAGGAGACACTT-3').

**Chemical reagents.** To reduce contractility, Bb(+), an inactive enantiomere of the selective inhibitor of myosin II ATPase activity, or Bb(-), the selective inhibitor (Tocris, 1853 and 1852), were diluted to 5, 12.5 or 25  $\mu$ M in KSOM from DMSO stocks. Y-27632 (Sigma, Y0503) in H<sub>2</sub>O stock was diluted to 10, 20 and 40  $\mu$ M in KSOM. To induce higher cortical tension, calyculin A (Sigma, C5552) in DMSO stock was diluted to 0.5 nM in KSOM, and lysophosphatidic acid (LPA, Sigma, L7260) was used at 20  $\mu$ M. To perturb mitosis, 2  $\mu$ g/ml of aphidicolin (Sigma, A0781) was used to arrest embryos at S-phase, and 50 nM of nocodazole was used to arrest embryos at metaphase. To reduce cell–cell adhesion, ECCD1 (ThermoFisher, no. 13-1800), an E-cadherin blocking antibody, was added to the medium 3 h before E3.5 at a final concentration of 50  $\mu$ g/ml. Note that when ECCD1 is added too early (E3.25), the embryos de-compact and do not form blastocysts; when ECCD1 is added at a time later than E3.5, there is no visible effect on cavity expansion and final size. To induce a smaller cavity, ouabain (Sigma, O3125), an inhibitor of the Na<sup>+</sup>/K<sup>+</sup> ATPase that establishes the osmotic gradient for blastocyst expansion, was used at 333  $\mu$ M. Alternatively, a final concentration of 100 mM of sucrose (Sigma, S1888) was added to KSOM (260 mOsm) to achieve hypertonic conditions (345 mOsm). Tight-junction inhibition was achieved using recombinant GST–C-CPE fusion protein (GST fused to the C-terminal half of CPE (amino acids 184–319)), an inhibitor of claudin4 and claudin6. GST–C-CPE and its inactive form, GST–C-CPE313 (GST fused to the C-terminal half of CPE313 (amino acids 184–313)), were diluted to 100  $\mu$ M before being applied to embryos

at E3.25. Embryos were incubated with drugs from E3.5 to E4.5, unless otherwise stated.

**GST–C-CPE and GST–C-CPE313 purification.** Plasmids encoding the C-CPE and its deletion mutant C-CPE313 were kindly provided by M. Furuse. GST-tagged C-CPE and C-CPE313 were expressed in *Escherichia coli* BL21 and purified as previously described<sup>13</sup>, with slight modifications. *E. coli* cells were sonicated in lysis buffer (50mM Tris, 300 mM NaCl, 5% glycerol, 1 mM DTT, 0.1% Triton X-100, protease inhibitor cocktail, DNase and 5mM MgCl<sub>2</sub>). The proteins were purified by GST beads (Protino Agarose Glutathione 4B, MACHEREY-NAGEL), followed by dialysis against PBS by using Slide-A-Lyzer Dialysis Cassettes, 3.5 kDa molecular mass cutoff (Thermo Fisher).

**Immunofluorescence staining.** Embryos were fixed using 1% PFA in PBS for 15 min at room temperature, washed with PBS added with Tween20 (Sigma, P7949) (PBST) and 3% BSA (Sigma, 9647), and permeabilized in 0.5% Triton X-100 (Sigma, T8787) in PBS. After washing, embryos were left in blocking solution (PBST with 5% BSA) for at least 4 h at 4°C and incubated overnight at 4°C with primary antibody diluted in washing buffer. After washing, embryos were incubated for one hour at room temperature in secondary antibody diluted in washing buffer. Embryos were then washed in washing buffer before imaging.

Primary antibodies against CDX2 (Sigma, SAB3500187) were used at 1:50. Primary antibodies against ZO1 (Invitrogen, 33-9100),  $\alpha$ -catenin (Abcam, ab51032), vinculin (Sigma, V9264), di-phosphorylated form (Thr18/Ser19) of the myosin regulatory light chain (Cell Signaling, 3674S), myosin heavy chain MYH9 (Cell Signaling, 3403P), E-cadherin (Sigma, U3254) and GATA4 (Santa Cruz Biotechnology, sc-9053) were used at 1:100. Primary antibody against occludin (Invitrogen, 71-1500) was used at 1:125. Primary antibodies against SOX2 (R&D Systems, AF2018) and CDX2 (Biogenex, MU392A-UC) were used at 1:200.

Secondary antibodies targeting mouse immunoglobulin coupled to Alexa Fluor 488 (Life Technologies, A21202), Alexa Fluor 555 (Life Technologies, A31570), rabbit immunoglobulin-coupled Alexa Fluor 546 (Invitrogen, A10040), rabbit immunoglobulin-coupled Alexa Fluor 488 (Life Technologies, A11008), goat immunoglobulin coupled to Alexa Fluor 488 (Life Technologies, A11055), goat immunoglobulin-coupled Alexa Fluor 555 (Life Technologies, A21432), rat immunoglobulin coupled to Alexa Fluor 633 (Invitrogen, A21094) and Cy5 targeting mouse immunoglobulin (Jackson ImmunoResearch, 715-175-150) were used at 1:200. DAPI (Invitrogen, D3751) was used at 1:2,000. Rhodamine-coupled phalloidin (Invitrogen, 1810954) was used at 1:500 and Alexa Fluor 633-coupled phalloidin (Invitrogen, R415) was used at 1:50.

**Tension measurement.** This method has been described in previous studies<sup>11</sup>. In brief, a microforged micropipette coupled to a microfluidic pump (Fluigent, MFCS) was used to measure the cortical tension of trophectoderm cells. To measure trophectoderm cortical tension at the 32- to 96-cell-stage (E3.5 to E4.5), micropipettes with radii of 4–6  $\mu$ m were used to apply stepwise increasing pressures on these cells, until a deformation with the same radius of the micropipette ( $R_p$ ) was reached. Care was taken to avoid aspirating cell cortex next to the cell nuclei, because cell nuclei are known to be stiff<sup>34</sup> and may introduce artefacts in the measured cortical tension. At steady state, the cortical tension  $\gamma$  of the blastomeres is calculated based on Young–Laplace's law:  $\gamma = P_c/2(1/R_p - 1/R_c)$ , in which  $P_c$  is the pressure used to deform the cell of radius  $R_c$ .

**Pressure measurement.** The 900A micropressure system (World Precision Instruments, SYS-900A) was used to make direct measurements of blastocoelic pressure, according to the manufacturer's instructions and as described in previous work<sup>9</sup>. In brief, a 0.5- or 1- $\mu$ m micropipette (World Precision Instruments, TIP05TW1E, TIP1TW1) was filled with 1 M KCl solution, placed in a microelectrode holder half-cell (World Precision Instruments, MEH6SF) and connected to a pressure source regulated by the 900A system. The microelectrode was calibrated using a calibration chamber (World Precision Instruments, CAL900A), before mounting it onto a micromanipulator (Narishige MON202-D) within an inverted Zeiss Axio Observer microscope. Blastocysts were first seeded onto dishes glued with coverslips (Thermo Scientific Menzel, 1130486) to provide a wedge against embryo movement during pressure measurement. The microelectrode was then inserted into the blastocyst and maintained in place for ~10 s before removal. Pressure measurement, which has a resolution of 13 Pa, was calculated as the mean pressure reading during this time interval. Data that show a rapid decrease in pressure within 10 s of probe insertion were discarded, as these indicate substantial leakage through rupture. The accuracy of the measured pressure from the micropressure system was validated by cross-checking with the cytoplasmic pressure of mouse oocytes (GV stage), which was calculated using Laplace's law:  $P_c = 2\gamma/R$ , in which  $\gamma$  is the cortical tension of the oocyte measured by micropipette aspiration, and  $R$  is the radius of the oocyte.

**Trophectoderm stiffness measurement.** To quantify tissue stiffness of trophectoderm epithelium, atomic force microscopy indentation measurements were carried out with a CellHesion 200 (JPK Instruments) mounted on a Nikon Ti inverted fluorescence microscope with 20×/NA 0.6 objective. A monodisperse polystyrene

bead (Cospheric, S-SLGMS-2.5, 50- $\mu\text{m}$  diameter) was glued onto a tipless silicon cantilever (Bruker MLCT-O10, spring constant: 0.03–0.05 N/m, confirmed by the thermal fluctuation method). Blastocysts were seeded onto poly-L-lysine-coated glass Petri dishes. Blastocysts were indented with a constant approach speed of 0.1  $\mu\text{m/s}$ , with a loading force of 5 to 10 nN. For each force-indentation curve, the apparent Young's modulus of the trophectoderm epithelium was determined (using MATLAB) by fitting the entire approach curve with a shell model<sup>19,35</sup>,

$$F = \frac{4}{3}E_s h^2 \varepsilon + \frac{16\pi}{3}E_s h R \varepsilon^3$$

in which  $E_s$  denotes the Young's modulus of the trophectoderm shell,  $R$  is the blastocyst radius,  $\varepsilon$  is the indentation strain defined as  $\varepsilon = d/2R$  (with  $d$  being the indentation depth).  $h$  is the monolayer thickness, which was measured as the average thickness of the trophectoderm cell–cell junctions. Images were taken before and after every indentation to ensure there was no leakage and blastocyst collapse induced by the indentation (images showing leakage were discarded from analysis). Independent experiments were performed at different dates to ensure reproducibility of results.

**Microscopy.** Tension measurements were performed on an inverted Zeiss Axio Observer microscope equipped with a dry 40 $\times$ /NA 0.75 Plan-Neofluar objective. For long-term time-lapse imaging of blastocyst development (E3.5–E4.5), a dry 20 $\times$ /0.8 PL Apo DICII objective was used. Images were captured by a Zeiss AxioCam MRm using Zeiss Axiovision software. The microscope was equipped with an incubation chamber to keep the sample at 37 °C. Confocal imaging of both fixed and live samples was performed using Zeiss LSM 780 Confocal Inverted Microscope with LD C-Apochromat 40 $\times$ /1.1 W Corr objective, using Zen 2012 LSM software. Laser lines used were: diode 405 nm, argon multi-line 458/488/514 nm, HeNe 561 nm and 633 nm. Laser power and digital gain settings were unchanged within a given session to permit direct comparison of expression levels among embryos stained in the same batch. Image stacks were acquired with axial step size of 1  $\mu\text{m}$  or less. Sequential image acquisitions were used to avoid bleed-through artefacts across different channels.

**Tight-junction permeability assay.** Embryos were first incubated in KSOM with 100  $\mu\text{M}$  FluoZinc (Thermo Fisher, F24194) for 8 h at the 32-cell stage to allow the dye to be loaded into the blastocoel by osmotic gradient. The embryos were then washed before being transferred to KSOM with 200  $\mu\text{M}$   $\text{ZnCl}_2$  and 100  $\mu\text{M}$  Ca-EDTA. Fluorescence intensity in the blastocyst cavity was first recorded, followed by the addition of either Bb(+) (control) or Bb(–) to the medium ( $t = 0$  min) and time-lapse imaging (every 5 min). Tight-junction permeability was then quantified by the presence or absence of increased fluorescence intensity within the blastocoel after 20 min. The sensitivity of the assay was verified in the control experiments, during which we occasionally observed a transient increase in the fluorescence signal within the blastocoel before blastocyst collapse, which indicates successful detection of junctional leaks.

To trace leakage sites in blastocysts undergoing collapse, embryos were first incubated in KSOM with 4-kDa fluorescein isothiocyanate (FITC)-dextran for 8 h at the 32-cell stage. The embryos were then washed in KSOM at the E4.5 blastocyst stage and imaged every 10 min. Upon seeing any mitotic cells in the blastocysts (visible metaphase plate in H2B–GFP expressing embryos), image acquisition was switched to fast mode to trace dye leakage sites across the entire blastocyst.

**Tracking of trophectoderm cell division and internalization during blastocyst development.** CDX2–GFP $\times$ H2B–mCherry mice were used to distinguish between trophectoderm and ICM cells during blastocyst development. Embryos at E3.5 (just before or at the initial phase of cavity expansion) were incubated in red DiI dye (ThermoFisher, C7000) at 1:100 dilution in KSOM for 30 min, before being washed and transferred to the imaging dish. DiI dye acts as a lineage tracer<sup>36</sup>, because it labels the outer trophectoderm cells and is inherited through the daughter cells in subsequent divisions. Consequently, all DiI-positive cells in the ICM must have originated from the labelled outer cells at E3.5 stage. The degree of internalization of outer cells into the ICM during blastocyst development is quantified as the ratio of DiI-positive ICM cells to the total number of ICM cells.

**Data analysis. Cell shape analysis.** Using FIJI, a circle was manually fit onto the cell–medium interface to extract the radius of curvature of the cell  $R_c$ . The diameter of the micropipette  $R_p$  was quantified by drawing a line perpendicular to the micropipette tip followed by the use of the linescan function. To quantify basal area and cell volume of trophectoderm cells during blastocyst expansion, embryos expressing mTmG were imaged with less than 1- $\mu\text{m}$  spacing of confocal slice. Trophectoderm cells near the equatorial plane of the blastocysts were picked for manual quantification of trophectoderm basal area. Following segmentation using a pathfinder algorithm (Dijkstra's algorithm), cell volume was calculated using the 3D ImageJ Suite plugin in FIJI.

**Time-lapse analysis.** A circle was manually fitted to the blastocyst cavity at the equatorial plane to extract the cavity diameter. Cavity volume was calculated assuming

spherical symmetry of the blastocyst cavity, which was confirmed by direct imaging of cavity shape using 4-kDa dextran–FITC dye. The steady-state cavity diameter was extracted from the maximum size reached during blastocyst development from E3.5 to E4.5. Volume expansion rate was calculated from the change in volume per hour in the final few hours before E4.5, excluding time points during the collapse phase. MATLAB was used to plot the temporal evolution of cavity diameter during blastocyst development.

**Quantification of inter-collapse interval.** To detect the blastocyst collapses, interpolating splines were fitted to the measured cavity diameter traces. Zero crossings of the first derivative then indicate switches from expansion to shrinkage. To exclude spurious diameter drops, the local minima of the first derivative were thresholded with  $s'_{\min} = -10 \mu\text{m h}^{-1}$ . For every trace, this method gives a series of collapse-event times:  $T_{\text{collapses}} = \{T_1, T_2, \dots, T_n\}$ . The empirical inter-collapse-interval distributions are then simply given by the respective time differences:  $\Delta T_i = T_{i+1} - T_i$ . The continuous inter-collapse interval densities shown in Fig. 1c (right) were obtained by Gaussian kernel density estimation of the log-transformed inter-collapse intervals; the kernel bandwidth was selected using Silverman's criteria<sup>37</sup>. The whole analysis was done with custom written Python scripts, using tools from the package SciPy.

**Intensity ratio measurements.** To quantify the signal intensity of vinculin and occludin, we used FIJI to draw a free-hand line with thickness  $\sim 1 \mu\text{m}$  along the junctions between two mural trophectoderm cells. After measuring the mean grey value for the intensity of the signal at the junctions, the same line was shifted to the cytoplasm of one of the two cells to measure the mean grey value for the cytoplasmic signal. The mean grey value for junctional signal was then normalized by the mean grey value for cytoplasmic signal. To track the change in CDX2 expression as trophectoderm cells internalize into the ICM, the mean signal intensity of CDX2–GFP and H2B–mCherry were quantified on a single middle  $z$ -slice through the nucleus using FIJI. The CDX2–GFP signal intensity was normalized to the H2B–mCherry signal to compensate for the decay of the signal along the  $z$ -axis, followed by normalization to the initial signal intensity at the initial time point.

**Line scan and skeletal analysis.** Using FIJI, we picked confocal slices near the equatorial plane of the blastocysts. We drew a line with thickness  $\sim 1 \mu\text{m}$  along the cell–cell junctions between two mural trophectoderm cells, starting from the most apical part of the tight junction towards the adherens junction. The mean intensity of the junctional or adherens markers was then plotted accordingly. For skeletal analysis, the continuity of signal for ppMRLC was analysed in mural trophectoderm cells of wild-type embryos fixed at E3.75 and E4.25. Phalloidin or ZO1 were co-stained as reference markers for junctional continuity. Maximum projections were performed for confocal slices that contained junctions of mural trophectoderm cells. Thresholding and binarization were applied before using the skeletonize function to extract the integrated density for ppMRLC and junctional marker.  $I_{\text{ppMRLC}}/I_{\text{junction}} < 1$  indicates punctate ppMRLC signal whereas  $I_{\text{ppMRLC}}/I_{\text{junction}} \approx 1$  indicates a continuous linear signal.

**Cell count.** Cell counts were performed using the modular interactive nuclear segmentation (MINS-1) package running on MATLAB, as described in a previous publication<sup>38</sup>. Multi-channel images containing the DAPI and CDX2 channels were pre-processed in FIJI to reduce cytoplasmic or zona pellucida noise before running MINS-1. The ICM cell number was obtained as the difference between the total cell number (from DAPI) and the trophectoderm cell number (CDX2<sup>+</sup> nuclei), and counter-checked with a manual count of SOX2<sup>+</sup> and GATA4<sup>+</sup> nuclei. **Statistics and reproducibility.** All statistical analysis was performed using Origin software (version 8.5.6, OriginLab).  $P$  values were calculated using two-tailed Mann–Whitney  $U$  test. All box plots extend from the 25th to 75th percentiles (horizontal box), with a line at the median and whiskers extending to maximum and minimum data points. No statistical methods were used to define sample size. Sample size was determined based on previous studies in the field. Each experiment was repeated at least three times using different batches of embryos on different days. Authors were not blinded during experiments and analysis because only viable embryos (based on correct morphology and cell number) were selected. After selection, the parameters for different experiments were measured at random. **Reporting summary.** Further information on research design is available in the Nature Research Reporting Summary linked to this paper.

## Data availability

Source Data for Figs. 1, 3, 5 and Extended Data Figs. 1, 2, 4, 5 are available in the online version of the paper. Any other relevant data are available from the corresponding authors upon reasonable request.

## Code availability

Code for theoretical model is available on GitHub at <https://github.com/truizherrero/Hydraulic-control-of-embryo-size>.

30. Tsunoda, Y., Yasui, T., Nakamura, K., Uchida, T. & Sugie, T. Effect of cutting the zona pellucida on the pronuclear transplantation in the mouse. *J. Exp. Zool.* **240**, 119–125 (1986).
31. Muzumdar, M. D., Tasic, B., Miyamichi, K., Li, L. & Luo, L. A global double-fluorescent Cre reporter mouse. *Genesis* **45**, 593–605 (2007).
32. Balbach, S. T. et al. Nuclear reprogramming: kinetics of cell cycle and metabolic progression as determinants of success. *PLoS ONE* **7**, e35322 (2012).
33. Vries, W. N. De et al. Expression of Cre recombinase in mouse oocytes : a means to study maternal effect genes. *Genesis* **112**, 110–112 (2016).
34. Guilak, F., Tedrow, J. R. & Burgkart, R. Viscoelastic properties of the cell nucleus. *Biochem. Biophys. Res. Commun.* **269**, 781–786 (2000).
35. Fery, A., Dubreuil, F. & Mohwald, H. Mechanics of artificial microcapsules. *New J. Phys.* **6**, 18 (2004).
36. Krupa, M. et al. Allocation of inner cells to epiblast vs primitive endoderm in the mouse embryo is biased but not determined by the round of asymmetric divisions (8→16- and 16→32-cells). *Dev. Biol.* **385**, 136–148 (2014).
37. Silverman, B. W. *Density Estimation for Statistics and Data Analysis* (CRC, 1996).
38. Lou, X., Kang, M., Xenopoulos, P., Muñoz-Descalzo, S. & Hadjantonakis, A. K. A rapid and efficient 2D/3D nuclear segmentation method for analysis of early mouse embryo and stem cell image data. *Stem Cell Reports* **2**, 382–397 (2014).

**Acknowledgements** We thank all laboratory members and the EMBL animal facility for support; M. Furuse for GST-C-CPE/CPE313 plasmids; A. Aulehla, D. Gilmour, F. Graner, E. Hannezo, S. Hopyan, P. Liberali, R. Prevedel and J. Solon for feedback; T. Higashi, A. Miller and C. Schwayer for the protocol on fluozin leakage assay. C.J.C. and G.M. are supported by EMBL Interdisciplinary Postdocs (EIPOD) fellowship under Marie Skłodowska-Curie Actions COFUND

(664726). T.H. is supported by EMBL, Deutsche Forschungsgemeinschaft (DFG) and the European Research Council (742732). T.R.-H. was supported by the Simons Foundation. L.M. thanks the MacArthur Foundation and the Radcliffe Institute for support. A.D.-M. is supported by EMBL and DFG (DI 2205/2-1).

**Author contributions** C.J.C. conceived the project, designed the experiments and wrote the manuscript with input from all authors. C.J.C. and M.C. performed and analysed all experiments; G.M. performed inter-collapse interval quantification; R.J.P. assisted with the initial setup of the micropressure system; M.B. and A.D.-M. assisted with atomic force microscopy measurements; T.R.-H. and L.M. created the theory, performed simulations and suggested experimental tests of the theory. L.M. contributed to the writing of the manuscript. T.H. supervised the study, helped to design the project, performed oocyte recovery and contributed towards writing the manuscript.

**Competing interests** The authors declare no competing interests.

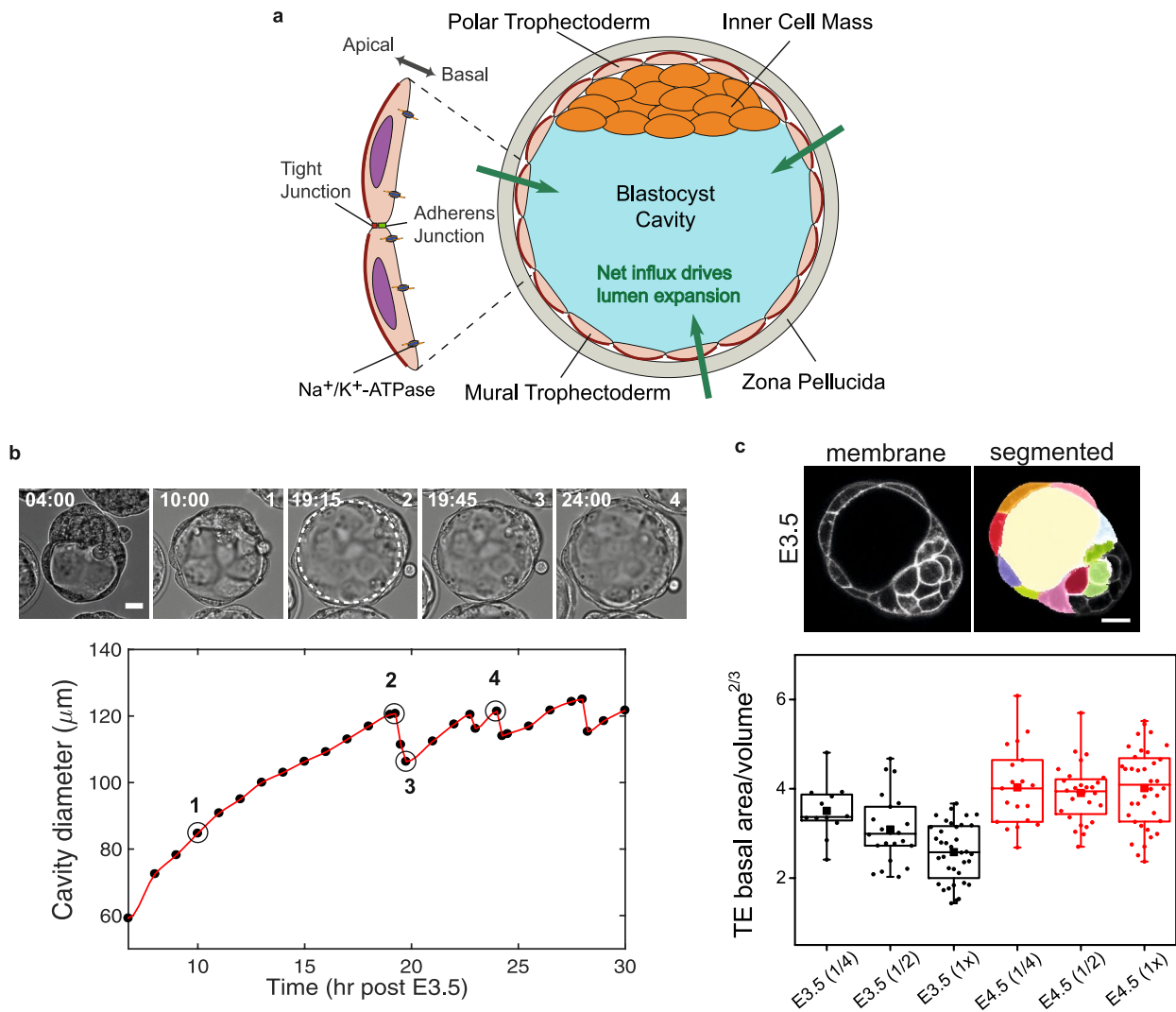
#### Additional information

**Supplementary information** is available for this paper at <https://doi.org/10.1038/s41586-019-1309-x>

**Correspondence and requests for materials** should be addressed to C.J.C. or L.M. or T.H..

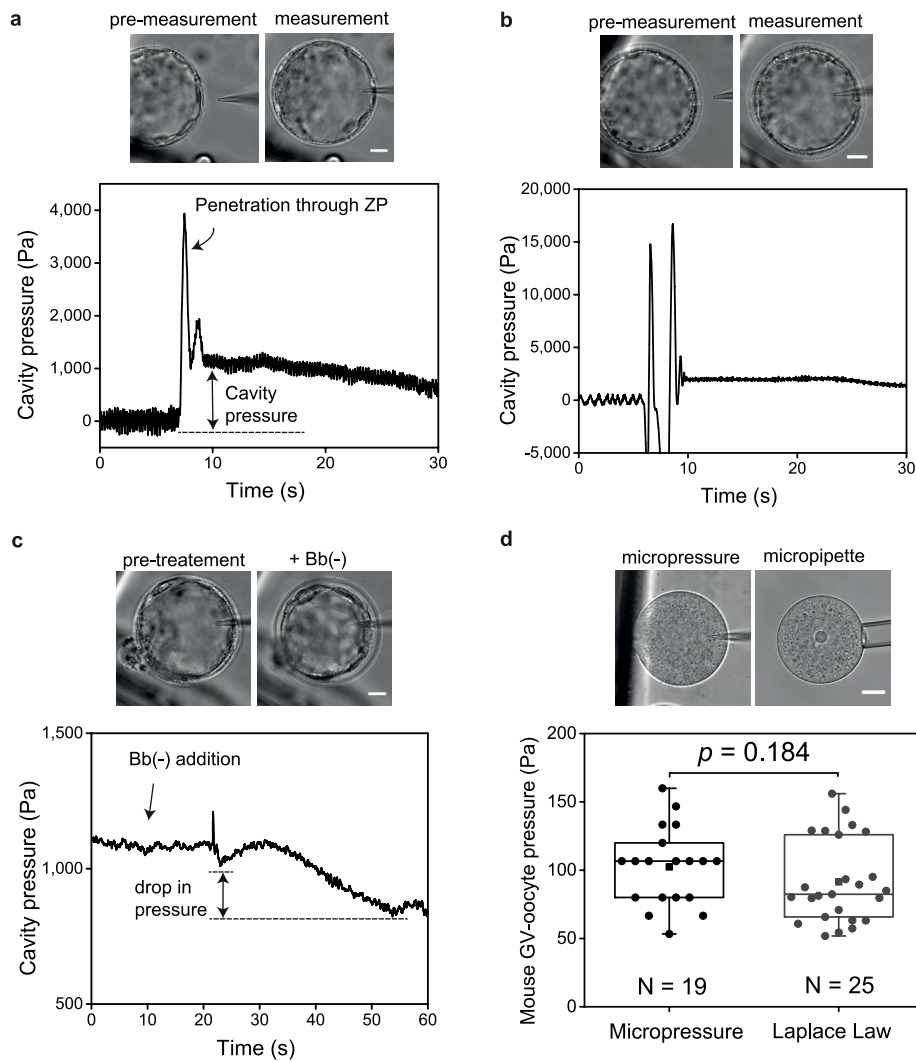
**Peer reviewer information** *Nature* thanks Shigeo Hayashi, Tristan A. Rodriguez and the other anonymous reviewer(s) for their contribution to the peer review of this work.

**Reprints and permissions information** is available at <http://www.nature.com/reprints>.



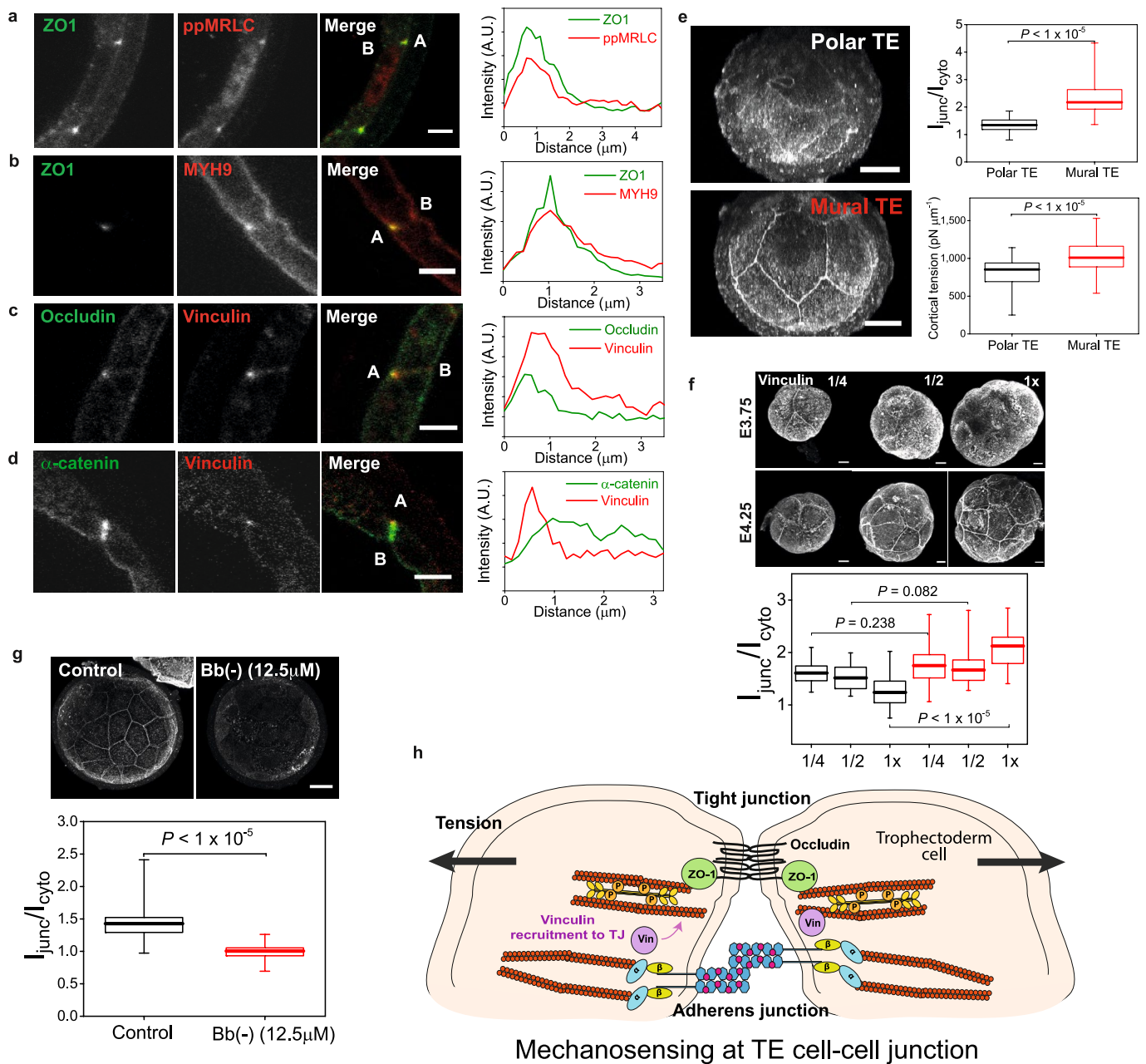
**Extended Data Fig. 1 | Blastocyst size is controlled by an embryo-autonomous mechanism.** **a**, Schematic representing mouse blastocyst development. The blastocyst, surrounded by a glycoprotein coat of the zona pellucida, is partitioned into the epithelial trophoblast, the ICM and the cavity. The outer trophoblast is further classified into the mural trophoblast (which surrounds the blastocyst cavity) and the polar trophoblast, which is in contact with the ICM. Apicobasal polarity is marked by the outer apical domains (red) and trophoblast cell-cell contacts with the apically localized tight junctions and adherens junctions. Na<sup>+</sup>/K<sup>+</sup>-ATPase pumps, enriched at the basolateral membrane of the trophoblast cells, help to establish an osmotic gradient across the trophoblast to drive fluid influx (green arrows). Together with the maturation of tight junctions that helps to seal the blastocyst against fluid outflow via paracellular junctions, blastocyst expansion then proceeds.

**b**, Images of embryos without zona pellucida undergoing blastocyst development (representative data from three independent experiments). The corresponding cavity diameter as a function of time (bottom) shows cycles of blastocyst collapse and re-expansion similar to those of embryos with intact zona-pellucida. Scale bar, 20 µm. Dotted line denotes the cavity. Time is shown as h:min after E3.5. **c**, Top, images of E3.5 blastocyst expressing mTmG (left) and after segmentation (right). Bottom, box plot showing trophoblast basal area normalized to cell volume in embryos of various sizes at the E3.5 (black,  $n = 11, 20$  and  $20$  embryos for 1/4, 1/2 and whole embryos, respectively) and E4.5 stages (red,  $n = 16, 21$  and  $22$  embryos for 1/4, 1/2 and whole embryos, respectively). Scale bar, 20 µm. Box plots show median, 25th and 75th percentiles, and whiskers extending to maximum and minimum data points.



**Extended Data Fig. 2 | Quantifying cavity pressure in mouse embryos using a micropressure probe.** **a, b,** Characteristics of successful cavity pressure measurements. Top, images showing two mouse blastocysts before and during pressure measurement. The baseline reading is close to zero when the microelectrode ( $0.5\ \mu\text{m}$ ) is not in contact with the blastocysts. A transient pressure spike is recorded as the tip of the microelectrode penetrates the zona pellucida. This is followed by a stable reading for about 5–10 s, before some potential leaks occur, which may cause a gradual drop in the reading with time. **c, d,** Proof-of-principle experiments to verify the pressure measurement. **c,** The addition of Bb(-)

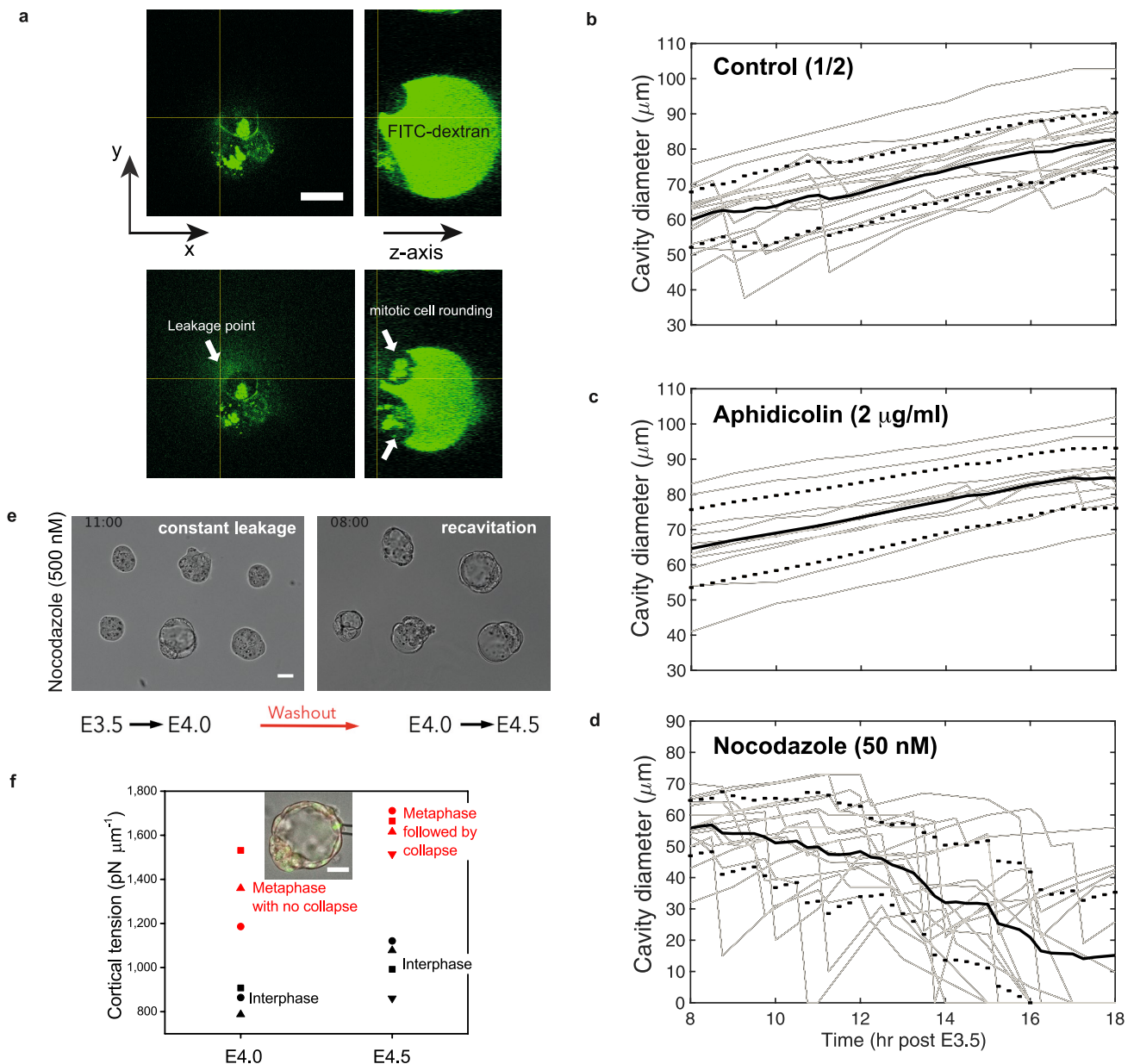
( $25\ \mu\text{M}$ ) leads to a transient reduction in cavity size and pressure within 10 s. **d,** The accuracy of the device was further demonstrated by comparing the cytoplasmic pressure of mouse oocytes at the germinal vesicle (GV) stage, measured directly by the micropressure probe and indirectly by Laplace's law through micropipette aspiration ( $P_c = 2\gamma/R$ , in which  $\gamma$  is the cortical tension of the oocyte measured by micropipette aspiration, and  $R$  is the radius of the oocyte). Data obtained by both approaches are not significantly different (Mann–Whitney  $U$  test). N, number of oocytes. Scale bars,  $20\ \mu\text{m}$ . All data show representative examples from three or more independent experiments.



**Extended Data Fig. 3 | Vinculin is recruited towards the tight junctions in a tension-dependent manner during blastocyst expansion.**

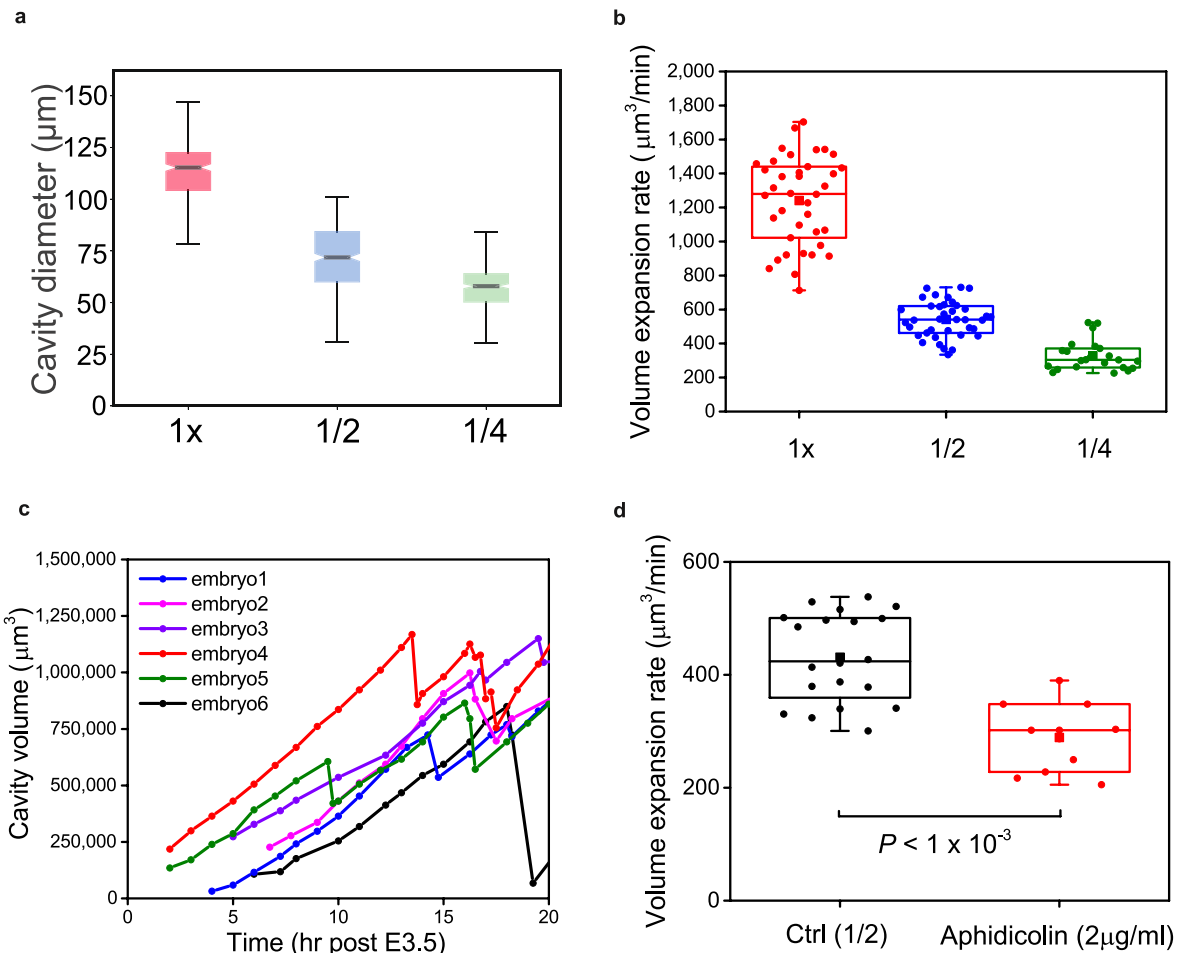
**a, b**, Immunostaining of wild-type embryos at the late blastocyst stage (E4.25), showing co-localization of ZO1 (green) with ppMRLC (red) (**a**) and MYH9 (red) (**b**). Line scans are shown on the right.  
**c, d**, Immunostaining of wild-type embryos at the late blastocyst stage (E4.25), showing co-localization of vinculin (red) with occludin (green) (**c**) and non-localization with  $\alpha$ -catenin (green) (**d**). Line scans are shown on the right. A and B mark the apical and basal sides of trophoblast cell-cell junctions. Scale bars, 5  $\mu\text{m}$ . **e**, Left, vinculin is more enriched at the mural trophoblast junctions than at the polar trophoblast junctions in E4.25 blastocysts (box plot shown at top right,  $n = 61$  cells from 11 embryos), which correlates with higher cortical tension in mural trophoblast cells compared to those of polar trophoblast cells (bottom right,  $n = 167$  cells from 25 embryos). Scale bars, 20  $\mu\text{m}$ . **f**, Top, immunostaining of blastocysts shows stronger signals of vinculin at trophoblast junctions of reduced blastocysts (1/4 and 1/2 blastocysts)

compared to whole embryos at E3.75, but equally strong signals in all blastocysts at E4.25. Scale bars, 10  $\mu\text{m}$ . Bottom, box plot of vinculin signal intensity in various blastocysts at E3.75 (black,  $n = 58$  cells from 15 embryos) and E4.25 (red,  $n = 54$  cells from 17 embryos). An overall higher intensity of vinculin at E4.25 across all blastocysts is consistent with the trend in trophoblast cortical tension (Fig. 1e). **g**, Immunostaining of vinculin in Bb(-)-treated and control embryos at the E4.25 stage. Bottom, box plot of vinculin signal intensity in control ( $n = 52$  cells from 11 embryos) versus Bb(-)-treated blastocysts ( $n = 28$  cells from 5 embryos). Scale bar, 20  $\mu\text{m}$ . **h**, Schematic depicting tension-dependent vinculin recruitment at tight junctions, possibly through actin binding, as trophoblast cells are increasingly stretched during cavity expansion. Mann-Whitney  $U$  test. All box plots show median, 25th and 75th percentiles, and whiskers extending to maximum and minimum data points. In **a-d**, representative examples from three independent experiments are shown.



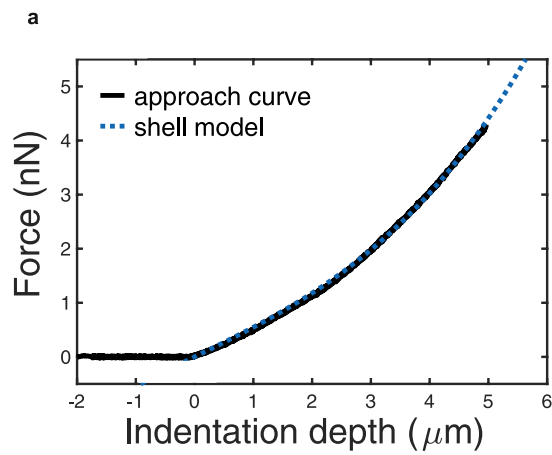
**Extended Data Fig. 4 | Leakage of blastocoel fluid during trophectoderm cell division leads to the collapse of blastocysts at mature stage.** **a**, Images of a blastocyst (at E4.25) showing blastocoel loaded with 4-kDa FITC-dextran dye, before (top) and after (bottom) collapse. Dye leakage following blastocyst collapse occurs preferentially at cell-cell junctions between mitotic trophoblast cells (white arrows). Scale bar, 20  $\mu\text{m}$ . **b-d**, Cavity diameter as a function of time (after E3.5) for 1/2 embryos treated with 2  $\mu\text{g ml}^{-1}$  of aphidicolin ( $n = 11$  embryos) (c) and 50 nM of nocodazole ( $n = 17$  embryos) (d) compared to control

1/2 embryos ( $n = 17$  embryos) (b). **e**, Images showing that nocodazole-treated 1/2 blastocysts that failed to expand upon initial collapse can re-cavitate upon washout. Scale bar, 30  $\mu\text{m}$ . **f**, Cortical tension of mural trophoblast cells measured during interphase (black) and metaphase (red) at mid- (E4.0) and late (E4.5) blastocyst stages. Different symbols correspond to the different cells being measured. Inset, image showing tension measurement for a trophoblast cell undergoing mitosis at E4.5 (green indicates nucleus at M-phase). In **a**, **e**, **f**, representative examples from three independent experiments are shown.

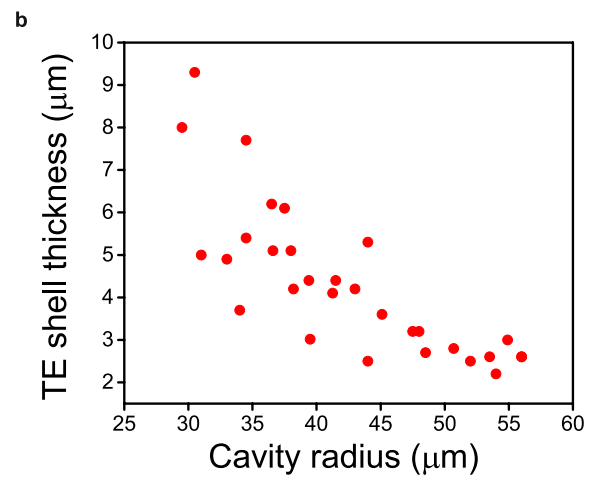


**Extended Data Fig. 5 | Expansion rates of the blastocyst cavity scale with the total cell number.** **a**, Cavity diameter at the plateau stage for whole blastocysts (without zona pellucida) and reduced blastocysts (1/2 blastocysts, blue; 1/4 blastocysts, green). **b**, Box plot of volume expansion rate for reduced and whole blastocysts shows that blastocysts expand at a rate that scales approximately with the initial number of cells. For **a**, **b**,  $n = 14$ , 21 and 16 embryos for whole, 1/2 and 1/4 embryos, respectively. **c**, Time evolution of cavity volume for six whole embryos (representative examples from four independent experiments). The slopes showed a

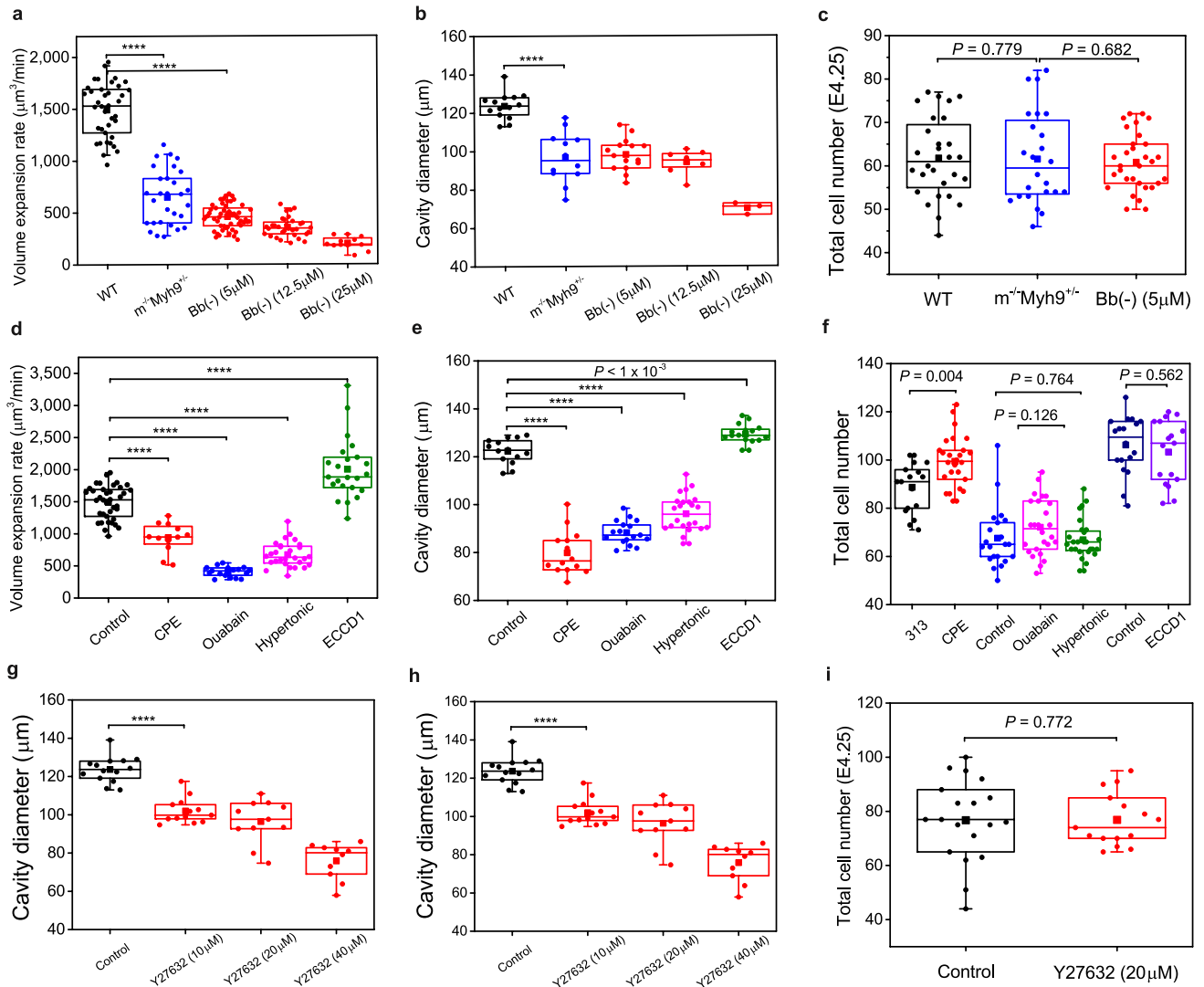
gradual increase with time as the cell number increased. **d**, Box plot of volume expansion rate for control 1/2 embryos ( $n = 20$  embryos) compared to 1/2 embryos ( $n = 11$  embryos) treated with aphidicolin ( $2\mu\text{g ml}^{-1}$ ), which arrests cells at S-phase entry. Mann-Whitney  $U$  test. Blastocysts with a reduced number of cells expressed fewer  $\text{Na}^+/\text{K}^+$ -ATPase pumps overall, which led to a reduced fluid influx and cavity expansion rate. Box plots show median line, 25th and 75th percentiles, and whiskers extending to maximum and minimum data points.



**Extended Data Fig. 6 | Measurement of apparent trophectoderm stiffness (Young's modulus) by atomic force microscopy.** **a**, Force-distance curve measured on a mature blastocyst (E4.25). Blastocysts were typically indented with a loading force of 5 to 10 nN. Data show representative examples from four independent experiments. Dashed line is the fit of the approach curve to the shell model (see Methods).

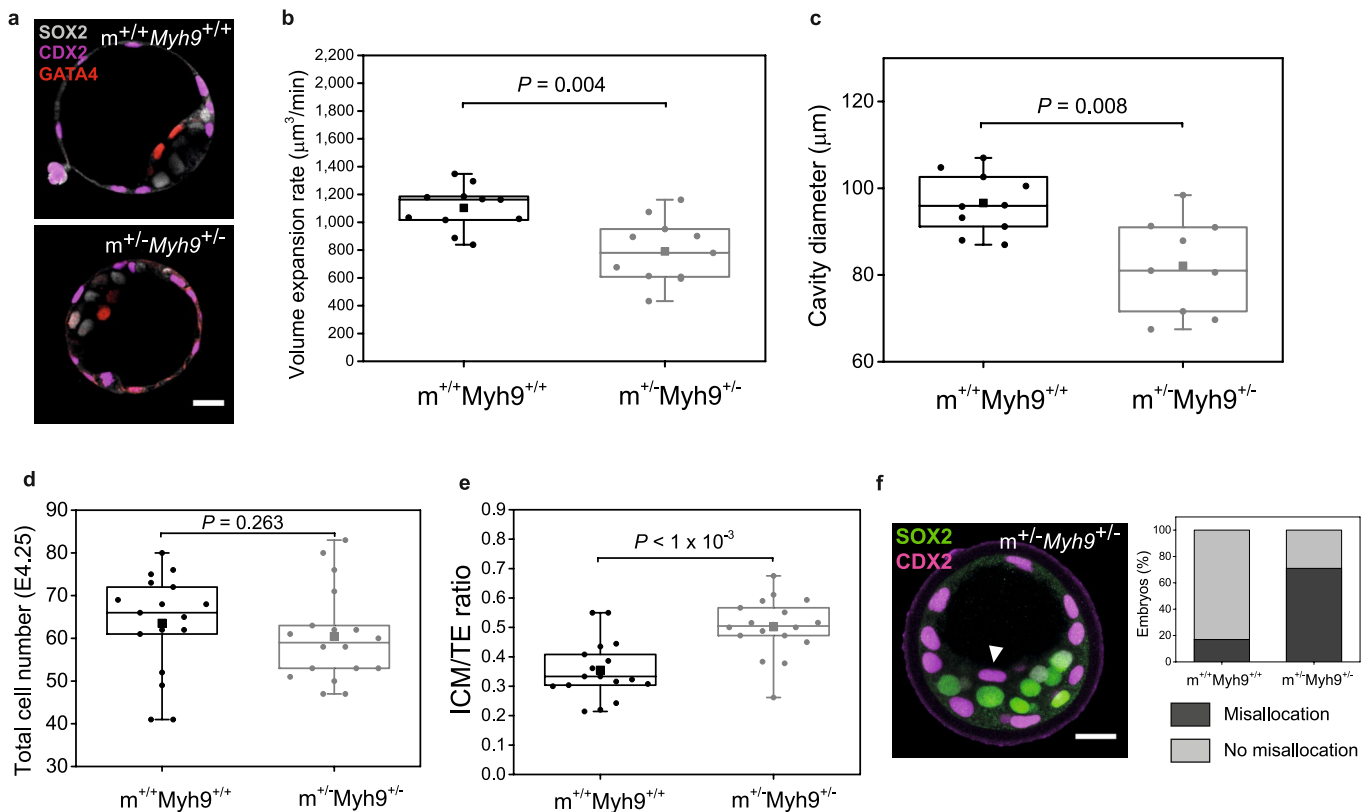


**b**, Measured trophectoderm epithelial thickness as a function of cavity radius. Data pooled from  $n = 31$  embryos in 4 independent experiments. The thinning of the trophectoderm shell is a natural consequence of blastocyst expansion, as predicted by the model (see Supplementary Notes). The value of individual trophectoderm shell thickness is used for fitting in **a**, to extract the apparent trophectoderm stiffness (see Methods).



**Extended Data Fig. 7 | Regulation of blastocyst size by cortical tension, tight-junction permeability, ion influx and cell-cell adhesion.** **a**, Dose-dependent volume expansion rate in  $Bb(-)$ -treated embryos (red,  $n = 15$ , 8 and 4 embryos for 5, 12.5 and 25  $\mu\text{M}$ , respectively) and  $m^{-/-}Myh9^{+/-}$  embryos (blue,  $n = 12$  embryos), compared to the wild type (black,  $n = 23$  embryos). **b**, **c**, Maximum cavity diameter reached for wild type (black,  $n = 14$  embryos),  $m^{-/-}Myh9^{+/-}$  (blue,  $n = 12$  embryos) and embryos treated with  $Bb(-)$  (red) in various concentrations ( $n = 15$ , 8 and 4 embryos for 5, 12.5 and 25  $\mu\text{M}$ , respectively) (**b**). These embryos all have similar numbers of cells (**c**), which shows that the reduced cavity size is not due to a reduced number of cells.  $n = 28$ , 24 and 31 embryos for wild-type,  $m^{-/-}Myh9^{+/-}$  and  $Bb(-)$ -treated embryos, respectively. **d**, Volume expansion rate in CPE- (red,  $n = 12$  embryos), ouabain- (blue,  $n = 17$  embryos), hypertonic- (pink,  $n = 28$  embryos) and ECCD1-treated (green,  $n = 23$  embryos) embryos compared to controls (black,  $n = 23$  embryos). **e**, Maximum cavity diameter for CPE- (red,  $n = 14$  embryos), ouabain- (blue,  $n = 17$  embryos), hypertonic- (pink,  $n = 25$  embryos) and

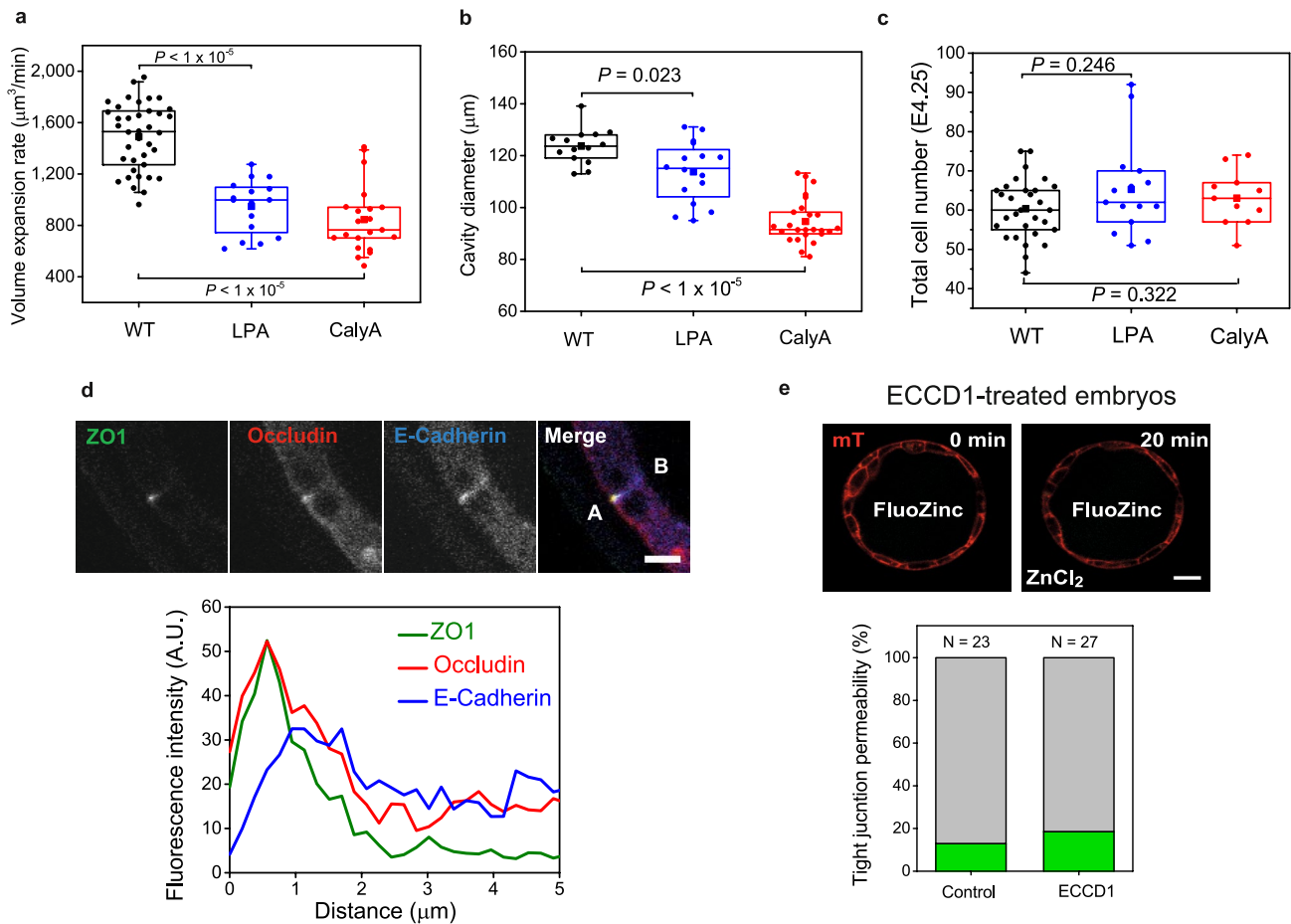
ECCD1-treated (green,  $n = 16$  embryos) embryos compared to controls (black,  $n = 14$  embryos). **f**, ECCD1-treated embryos have similar numbers of cells to those of controls (dark blue, E5.0), whereas CPE-treated embryos have slightly higher numbers of cells than do control embryos (black, E4.25), despite their reduced cavity size.  $n = 17$  and 26 embryos for 313 (CPE131, used as control) and CPE-treated embryos;  $n = 21$ , 26 and 28 embryos for control, ouabain- and hypertonic-treated embryos; and  $n = 18$  and 17 embryos for control and ECCD1-treated embryos, respectively. **g**–**i**, Embryos treated with Y-27632 (a Rho-kinase inhibitor that targets actomyosin contractility) showed a reduced expansion rate (**g**) and cavity size (**h**), despite having cell numbers that were similar to those of controls (**i**).  $n = 14$ , 13, 11 and 10 embryos for controls, 10, 20 and 40  $\mu\text{M}$  Y-27632-treated embryos, respectively, in **g** and **h**;  $n = 19$  and 15 for control and Y-27632-treated embryos, respectively, in **i**. All box plots show median line, 25th and 75th percentiles, and whiskers extending to maximum and minimum data points. Mann–Whitney  $U$  test. \*\*\*\*  $P < 1 \times 10^{-5}$ .



**Extended Data Fig. 8 | Maternal heterozygous knockout and zygotic heterozygous ( $m^{+/-}Myh9^{+/-}$ ) embryos exhibit smaller cavity and increased ICM compared to wild type in the same littermate.**

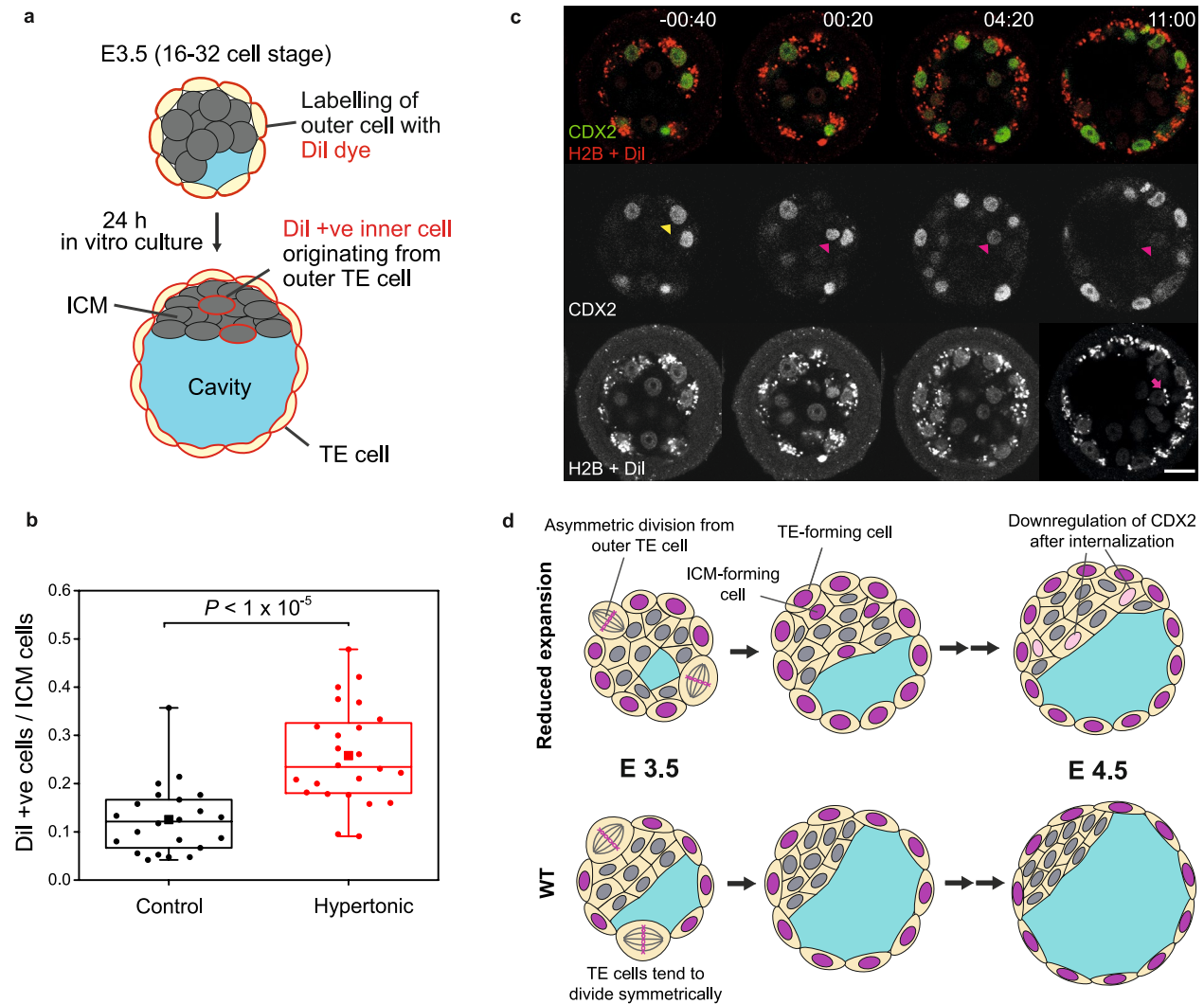
**a**, Immunostaining of late-stage (E4.25)  $m^{+/-}Myh9^{+/-}$  and wild-type embryos in the same littermate ( $m^{+/+}Myh9^{+/+}$ ), showing trophoblast (CDX2, magenta), epiblast (SOX2, grey) and primitive endoderm (GATA4, red) fates. Data are a representative example from three independent experiments. Scale bar, 20  $\mu\text{m}$ . **b–e**, Volume expansion rate for  $m^{+/-}Myh9^{+/-}$  ( $n = 11$  embryos) is significantly lower than that of  $m^{+/+}Myh9^{+/+}$  ( $n = 11$  embryos) embryos (**b**), which leads to a smaller

cavity size (**c**) and higher ratio of ICM to trophectoderm (**e**), despite the range in cell number being similar for both genotypes (**d**).  $n = 17$  and 18 embryos for  $m^{+/+}Myh9^{+/+}$  and  $m^{+/-}Myh9^{+/-}$  embryos, respectively, in **d** and **e**. **f**, Immunostaining of  $m^{+/-}Myh9^{+/-}$  embryos (E4.25) showing misallocation of CDX2-expressing cells in the ICM (white arrowhead). Scale bar, 20  $\mu\text{m}$ . Right, quantification of lineage misallocation in  $m^{+/-}Myh9^{+/-}$  embryos.  $n = 35$  and 24 embryos for  $m^{+/+}Myh9^{+/+}$  and  $m^{+/-}Myh9^{+/-}$  embryos, respectively. All box plots show median line, 25th and 75th percentiles, and whiskers extending to maximum and minimum data points. Mann-Whitney  $U$  test.



**Extended Data Fig. 9 | Increased cortical tension leads to reduced cavity expansion rate and size, whereas ECCD1 treatment preserves tight junctions.** **a**, Volume expansion rate in embryos treated with 20  $\mu\text{M}$  lysophosphatidic acid (LPA,  $n = 16$  embryos), and 0.5 nM calyculin A (CalyA,  $n = 21$  embryos) compared to wild type ( $n = 38$ ). LPA and calyculin A are known to activate cortical contractility. **b**, Maximum cavity diameter reached for wild type ( $n = 14$  embryos), LPA ( $n = 16$  embryos) and calyculin A ( $n = 25$  embryos). **c**, Total cell number for wild type ( $n = 30$  embryos) and embryos treated with LPA ( $n = 15$  embryos) and calyculin A ( $n = 11$  embryos) is similar, which indicates that the reduced expansion rate and cavity size is not due to a reduced cell-proliferation rate. Box plots show median line, 25th and 75th percentiles, and whiskers extending to maximum and minimum data points. Mann-Whitney  $U$

test. **d**, **e**, Tight junctions remain sealed and functional, despite impaired functions of adherens junctions. **d**, Top, immunostaining of E5.0 embryos treated with 50  $\mu\text{g ml}^{-1}$  of ECCD1 (representative example from three independent experiments). A and B indicate the apical and basal sides of cell-cell junctions, respectively. Bottom, corresponding line scans show that tight junctions appear intact, as shown by the decoupling of signals of ZO1 and occludin from E-cadherin. A.U., arbitrary units. Scale bar, 5  $\mu\text{m}$ . **e**, Top, tight-junction leakage assay shows that an ECCD1-treated embryo loaded with fluozinc (100  $\mu\text{M}$ ) displayed no increase in fluorescence intensity within the cavity when ZnCl<sub>2</sub> (200  $\mu\text{M}$ ) was added. Bottom, percentage of blastocysts showing no difference in permeability (green) in ECCD1-treated embryos compared to control embryos.  $N$ , number of embryos. Scale bar, 20  $\mu\text{m}$ .



**Extended Data Fig. 10 | Reduced lumen expansion biases cell allocation towards the ICM through increased asymmetric division of outer cells.** **a**, Schematic depicting a DiI dye assay that assesses how outer trophoblast (TE) cells contribute to the ICM through asymmetric divisions. **b**, Box plot of ratios of DiI-positive cell number within the ICM to the total ICM cell number, in control ( $n = 22$  embryos) and hypertonic-treated embryos ( $n = 24$  embryos). Box plot shows median line, 25th and 75th percentiles, and whiskers extending to maximum and minimum data points. Mann-Whitney  $U$  test. **c**, Time-lapse images of hypertonic-treated CDX2-GFP $\times$ H2B-mCherry embryo labelled with DiI dye, during blastocyst expansion. An outer cell (yellow arrowhead) undergoes asymmetric division to generate one trophoblast-forming

and one ICM-forming cell; the latter carries the DiI signal (magenta arrow) as it internalizes into the ICM. CDX2 (but not H2B) expression is downregulated (magenta arrowhead) following internalization, whereas CDX2 expression in the outer cells remains constant or increases throughout blastocyst development. Data show a representative example from three independent experiments. Time is shown as h:min after nuclear envelope breakdown. Scale bar, 20  $\mu$ m. **d**, Schematic represents how lumenal expansion affects cell positioning and fate acquisition. Reduced lumenal expansion increases the frequency of asymmetric division of outer cells, which generates a trophoblast- and an ICM-forming cell; the latter eventually acquires ICM fate.

## Reporting Summary

Nature Research wishes to improve the reproducibility of the work that we publish. This form provides structure for consistency and transparency in reporting. For further information on Nature Research policies, see [Authors & Referees](#) and the [Editorial Policy Checklist](#).

### Statistics

For all statistical analyses, confirm that the following items are present in the figure legend, table legend, main text, or Methods section.

n/a Confirmed

- |                                     |                                     |  |
|-------------------------------------|-------------------------------------|--|
| <input type="checkbox"/>            | <input checked="" type="checkbox"/> | The exact sample size ( $n$ ) for each experimental group/condition, given as a discrete number and unit of measurement  |
| <input type="checkbox"/>            | <input checked="" type="checkbox"/> | A statement on whether measurements were taken from distinct samples or whether the same sample was measured repeatedly  |
| <input type="checkbox"/>            | <input checked="" type="checkbox"/> | The statistical test(s) used AND whether they are one- or two-sided<br><i>Only common tests should be described solely by name; describe more complex techniques in the Methods section.</i>   |
| <input checked="" type="checkbox"/> | <input type="checkbox"/>            | A description of all covariates tested   |
| <input checked="" type="checkbox"/> | <input type="checkbox"/>            | A description of any assumptions or corrections, such as tests of normality and adjustment for multiple comparisons  |
| <input type="checkbox"/>            | <input checked="" type="checkbox"/> | A full description of the statistical parameters including central tendency (e.g. means) or other basic estimates (e.g. regression coefficient) AND variation (e.g. standard deviation) or associated estimates of uncertainty (e.g. confidence intervals) |
| <input type="checkbox"/>            | <input checked="" type="checkbox"/> | For null hypothesis testing, the test statistic (e.g. $F$ , $t$ , $r$ ) with confidence intervals, effect sizes, degrees of freedom and $P$ value noted<br><i>Give <math>P</math> values as exact values whenever suitable.</i>                            |
| <input checked="" type="checkbox"/> | <input type="checkbox"/>            | For Bayesian analysis, information on the choice of priors and Markov chain Monte Carlo settings   |
| <input checked="" type="checkbox"/> | <input type="checkbox"/>            | For hierarchical and complex designs, identification of the appropriate level for tests and full reporting of outcomes   |
| <input type="checkbox"/>            | <input checked="" type="checkbox"/> | Estimates of effect sizes (e.g. Cohen's $d$ , Pearson's $r$ ), indicating how they were calculated   |

*Our web collection on [statistics for biologists](#) contains articles on many of the points above.*

### Software and code

Policy information about [availability of computer code](#)

Data collection

Zeiss Axiovision and Zeiss ZEN software were used for time-lapsing microscopy and tension measurement. Imaging on immunostained samples were done using Zeiss Zen software.  
LabScribe 2 software was used for pressure measurement.

Data analysis

Statistical analysis was performed using the software Origin (version 8.5.6; OriginLab). ImageJ was used to quantify imaging data. Cell count was performed using Modular Interactive Nuclear Segmentation (MINS-1) package running on MATLAB. version 9.1.0.441655 (R2016b). Fit to tissue elasticity was done with MATLAB. version 9.1.0.441655 (R2016b). The inter-collapse interval was analyzed using custom written Python scripts, using tools from the scientific package SciPy. Custom made codes can be made available upon request to the corresponding authors. Code for theoretical simulation is available on GitHub at <https://github.com/truizherrero/Hydraulic-control-of-embryo-size>.

For manuscripts utilizing custom algorithms or software that are central to the research but not yet described in published literature, software must be made available to editors/reviewers. We strongly encourage code deposition in a community repository (e.g. GitHub). See the Nature Research [guidelines for submitting code & software](#) for further information.

### Data

Policy information about [availability of data](#)

All manuscripts must include a [data availability statement](#). This statement should provide the following information, where applicable:

- Accession codes, unique identifiers, or web links for publicly available datasets
- A list of figures that have associated raw data
- A description of any restrictions on data availability

Source data supporting the findings are available online as Supplementary Data.

## Field-specific reporting

Please select the one below that is the best fit for your research. If you are not sure, read the appropriate sections before making your selection.

Life sciences     Behavioural & social sciences     Ecological, evolutionary & environmental sciences

For a reference copy of the document with all sections, see [nature.com/documents/nr-reporting-summary-flat.pdf](https://www.nature.com/documents/nr-reporting-summary-flat.pdf)

## Life sciences study design

All studies must disclose on these points even when the disclosure is negative.

Sample size	No particular statistical method was used to define sample size. Sample size was determined based on previous studies in the field. A minimum of 3 independent experiments were carried out.
Data exclusions	For pressure measurement, data that show a rapid decrease in pressure within 10 s after probe insertion were discarded as they indicate significant leakage through rupture. For analysis on ICM/TE ratio, Myh9 deleted mutants that had very low cell number (compromised viability) are excluded from the analysis.
Replication	Experiments were reliably reproduced. At least 3 independent experiments were carried out. Experiments were performed on different days with different batches of embryos.
Randomization	After selecting embryos for proper morphology/viability, the parameters for different experiments were measured at random.
Blinding	Authors were not blinded because embryos were selected prior to analysis. Criteria for selection was embryo viability and proper morphology.

## Reporting for specific materials, systems and methods

We require information from authors about some types of materials, experimental systems and methods used in many studies. Here, indicate whether each material, system or method listed is relevant to your study. If you are not sure if a list item applies to your research, read the appropriate section before selecting a response.

### Materials & experimental systems

n/a	Involved in the study
<input type="checkbox"/>	<input checked="" type="checkbox"/> Antibodies
<input checked="" type="checkbox"/>	<input type="checkbox"/> Eukaryotic cell lines
<input checked="" type="checkbox"/>	<input type="checkbox"/> Palaeontology
<input type="checkbox"/>	<input checked="" type="checkbox"/> Animals and other organisms
<input checked="" type="checkbox"/>	<input type="checkbox"/> Human research participants
<input checked="" type="checkbox"/>	<input type="checkbox"/> Clinical data

### Methods

n/a	Involved in the study
<input checked="" type="checkbox"/>	<input type="checkbox"/> ChIP-seq
<input checked="" type="checkbox"/>	<input type="checkbox"/> Flow cytometry
<input checked="" type="checkbox"/>	<input type="checkbox"/> MRI-based neuroimaging

## Antibodies

### Antibodies used

#### Primary antibodies:

Mouse mAb Anti-ZO1 (Invitrogen, 33-9100) used at 1:100.  
Rabbit mAb Anti- $\alpha$ -catenin (Abcam, ab51032) used at 1:100.  
Mouse mAb Anti-vinculin (Sigma, V9264) used at 1:100.  
Rabbit pAb Anti-di-phosphorylated form (Thr18/Ser19) of myosin regulatory light chain (Cell Signaling, 3674S).  
Rabbit pAb Anti-myosin heavy chain Myh9 (Cell Signaling, 3403P) used at 1:100.  
Rabbit pAb Anti-occludin (Invitrogen, 71-1500) used at 1:125.  
Rat mAb Anti-Uvomorulin / E-Cadherin (Sigma Aldrich, U3254) used at 1:100.  
Rabbit pAb Anti-Gata-4 (Santa Cruz Biotechnology, sc-9053) used at 1:100.  
Goat pAb Anti-Sox2 (R&D Systems, AF2018) used at 1:200.  
Rabbit mAb Anti-Cdx2 (Sigma Aldrich, SAB3500187) used at 1:50.  
Mouse mAb Anti-Cdx2 (Biogenex, MU392A-UC) used at 1:200.

#### Secondary antibodies:

Alexa Fluor 488 Donkey Anti-mouse (Life technologies, A21202) used at 1:200.  
Alexa Fluor 555 Donkey Anti-mouse (Life Technologies, A31570) used at 1:200.  
Alexa Fluor 546 Donkey Anti-rabbit (Invitrogen, A10040) used at 1:200.  
Alexa Fluor 488 Goat Anti-rabbit (Life Technologies, A11008) used at 1:200.  
Alexa Fluor 488 Donkey Anti-goat (Life Technologies, A11055) used at 1:200.  
Alexa Fluor 555 Donkey Anti-goat (Life Technologies, A21432) used at 1:200.  
Alexa Fluor 633 Goat Anti-rat (Invitrogen, A21094) used at 1:200.  
Cy5 Donkey Anti-mouse (Jackson ImmunoResearch, 715-175-150) used at 1:200.

## Validation

Also stated in the methods section under Immunofluorescence staining.

Antibody validations were performed by antibody suppliers or were published in earlier studies. Relevant articles are:

Mouse anti-ZO1 (Invitrogen, 33-9100)

Nagasaka et al., "Differences in the Mechanical Properties of the Developing Cerebral Cortical Proliferative Zone between Mice and Ferrets at both the Tissue and Single-Cell Levels", *Frontiers in Cell and Developmental Biology*, 4:139, (2016).

Reginensi et al., "A critical role for NF2 and the Hippo pathway in branching morphogenesis", *Nature communications*, 7:12309, (2016).

Ichise et al., "Phospholipase C $\gamma$ 2 Is Required for Luminal Expansion of the Epididymal Duct during Postnatal Development in Mice", *PLoS one*, 11(3): e0150521, (2016).

Rabbit anti- $\alpha$ -catenin (Abcam, ab51032)

Dietrich J.-E. et al., "Venus trap in the mouse embryo reveals distinct molecular dynamics underlying specification of first embryonic lineages", *EMBO Rep.* 16:1005-21 (2015).

Wu M. et al., "Epicardial Spindle Orientation Controls Cell Entry into the Myocardium", *Dev Cell*, 19:114-125 (2010).

Mouse anti-vinculin (Sigma, V9264)

Binamé F. et al., "Cancer-associated mutations in the protrusion-targeting region of p190RhoGAP impact tumor cell migration", *J Cell Biol.*, 214(7):859-73 (2016).

Elosegui-Artola A. et al., "Mechanical regulation of a molecular clutch defines force transmission and transduction in response to matrix rigidity", *Nat Cell Biol.*, 18(5):540-8 (2016).

Elloumi-Hannachi I. et al., "Contributions of the integrin  $\beta$ 1 tail to cell adhesive forces", *Exp Cell Res.*, 332(2):212-22 (2015).

Rabbit anti-di-phosphorylated form (Thr18/Ser19) of myosin regulatory light chain (Cell Signaling, 3674)

Maître, J. L., Niwayama, R., Turlier, H., Nedelec, F. & Hiiragi, T. Pulsatile cell-autonomous contractility drives compaction in the mouse embryo. *Nat. Cell Biol.* 17, 849–855 (2015).

Maître, J. L. et al. Asymmetric division of contractile domains couples cell positioning and fate specification. *Nature* 536, 344–348 (2016).

Rabbit anti-myosin heavy chain Myh9 (Cell Signaling, 3403)

Maître, J. L., Niwayama, R., Turlier, H., Nedelec, F. & Hiiragi, T. Pulsatile cell-autonomous contractility drives compaction in the mouse embryo. *Nat. Cell Biol.* 17, 849–855 (2015).

Maître, J. L. et al. Asymmetric division of contractile domains couples cell positioning and fate specification. *Nature* 536, 344–348 (2016).

Rabbit anti-occludin (Invitrogen, 71-1500)

Sheng Z.Y. et al., "Sertoli Cells Are Susceptible to ZIKV Infection in Mouse Testis", *Front Cell Infect Microbiol.*, 7:272 (2017).

Whiteman E.L. et al., "Crumbs3 is essential for proper epithelial development and viability", *Mol Cell Biol.*, 34(1):43-56 (2014).

Xiao X. et al., "N-wasp is required for structural integrity of the blood-testis barrier", *PLoS Genet.*, 10(6): e1004447 (2014).

Rat anti-Uvomorulin / E-Cadherin (Sigma Aldrich, U3254)

Samarage C.R. et al., "Cortical Tension Allocates the First Inner Cells of the Mammalian Embryo", *Dev Cell.*, 34(4):435-47 (2015).

Bessonard S. et al., "PC7 and the related proteases Furin and Pace4 regulate E-cadherin function during blastocyst formation", *J Cell Bio.*, 210 (7): 1185 (2015).

Trichas G. et al., "Nodal Dependent Differential Localisation of Dishevelled-2 Demarcates Regions of Differing Cell Behaviour in the Visceral Endoderm", *PLoS Biol.*, 9(2): e1001019 (2011).

Rabbit anti-Gata4 (Santa Cruz Biotechnology, sc-9053)

Posfai E. et al., "Position- and Hippo signaling-dependent plasticity during lineage segregation in the early mouse embryo", *eLife*, 6: e22906 (2017).

Thamodaran V. et al., "p38 (Mapk14/11) occupies a regulatory node governing entry into primitive endoderm differentiation during preimplantation mouse embryo development", *Open Biol.*, 6(9): 160190 (2016).

Le Bin G.C. et al., "Oct4 is required for lineage priming in the developing inner cell mass of the mouse blastocyst", *Development*, 141(5):1001-10 (2014).

Goat anti-Sox2 (R&D Systems, AF2018)

Yao C. et al., "Sin3a regulates epithelial progenitor cell fate during lung development", *Development*, 144(14):2618-2628 (2017).

You L. et al., "Deficiency of the chromatin regulator BRPF1 causes abnormal brain development", *J Biol Chem.*, 290(11):7114-29 (2015).

Schrode N. et al., "GATA6 levels modulate primitive endoderm cell fate choice and timing in the mouse blastocyst", *Dev Cell.*, 29(4):454-67 (2014).

Rabbit anti-Cdx2 (Sigma, SAB3500187)

Wen D. et al., "Completely ES cell-derived mice produced by tetraploid complementation using inner cell mass (ICM) deficient blastocysts", *PLoS One*, 9(4): e94730 (2014).

Mouse anti-Cdx2 (Biogenex, MU392A-UC)

Korotkevich, E. et al. The apical domain is required and sufficient for the first lineage segregation in the mouse embryo. *Dev. Cell* 40, 235–247.e7 (2017).

Maître, J. L. et al. Asymmetric division of contractile domains couples cell positioning and fate specification. *Nature* 536, 344–348 (2016).

Dietrich, J.-E. et al. Venus trap in the mouse embryo reveals distinct molecular dynamics underlying specification of first

## Animals and other organisms

Policy information about [studies involving animals](#); [ARRIVE guidelines](#) recommended for reporting animal research

### Laboratory animals

Embryos were recovered from superovulated female mice mated with male mice. Superovulation was induced by intraperitoneal injection of 5 international units (IU) of pregnant mare's serum gonadotropin (PMSG; Intervet Intergonan), followed by intraperitoneal injection of 5 IU human chorionic gonadotropin (hCG; Intervet Ovogest 1500) 44-48h later. Embryos were recovered both at the 2-cell-stage (E1.5) or at the 8-cell-stage (E2.5) by flushing oviducts from plugged females with 37°C KSOMaa with Hepes (Zenith Biotech, ZEHP-050, 50mL) using a custom-made syringe (Acufirm, 1400 LL 23). Embryos were handled using an aspirator tube (Sigma, A5177-5EA) equipped with glass pipettes pulled from glass micropipettes (Blaubrand intraMark). For in vitro culture, embryos were transferred to 10µl droplets of KSOM (Millipore, MR-121-D) in a tissue culture dish (Falcon, 353001) covered with mineral oil (Sigma, M8410 or Acros Organics), and cultured in an incubator with a humidified atmosphere supplemented with 5% CO<sub>2</sub> at 37°C.

### Wild animals

This study did not involve wild animals.

### Field-collected samples

This study did not involve samples collected from the field.

### Ethics oversight

Animal work was performed in the animal facility at the European Molecular Biology Laboratory, with permission from the institutional veterinarian overseeing the operation (ARC number TH11 00 11). The animal facilities are operated according to international animal welfare rules (Federation for Laboratory Animal Science Associations guidelines and recommendations).

Note that full information on the approval of the study protocol must also be provided in the manuscript.